

1 **Dissimilar Roles of Aerosols, Nitrogen Deposition and Ozone on the Terres-**  
2 **trial Carbon Sink in China during 2010-2020**

3 Nanhong Xie<sup>1</sup>, Tijian Wang<sup>1\*</sup>, Shu Li<sup>1</sup>, Bingliang Zhuang<sup>1</sup>, Mengmeng Li<sup>1</sup>, Min Xie<sup>2</sup>,  
4 Qian Zhang<sup>1</sup>, Danyang Ma<sup>2</sup>, Jane Liu<sup>3</sup>, Jing M. Chen<sup>3</sup>, Zhaozhong Feng<sup>4</sup>, Dimitrios Me-  
5 las<sup>5</sup>, Kostas Karatzas<sup>6</sup>

6 <sup>1</sup>School of Atmospheric Sciences, Nanjing University, Nanjing, China

7 <sup>2</sup>School of Environment, Nanjing Normal University, Nanjing, China

8 <sup>3</sup>Department of Geography and Planning, University of Toronto, Toronto, Ontario, Canada

9 <sup>4</sup>Key Laboratory of Ecosystem Carbon Source and Sink, China Meteorological Administra-  
10 tion (ECSS-CMA), School of Ecology and Applied Meteorology, Nanjing University of In-  
11 formation Science and Technology, Nanjing, China

12 <sup>5</sup>Laboratory of Atmospheric Physics, School of Physics, Aristotle University of Thessaloniki,  
13 Thessaloniki, Greece

14 <sup>6</sup>Environmental Informatics Research Group, School of Mechanical Engineering, Aristotle  
15 University of Thessaloniki, Thessaloniki, Greece

16

17 *Corresponding to:* Tijian Wang ([tjwang@nju.edu.cn](mailto:tjwang@nju.edu.cn))

18

19 **Abstract**

20 China's Clean Air Action (CAA) plan implemented since 2013 has significantly altered atmos-  
21 pheric composition, and yet its impact on the terrestrial carbon sink remains unclear. This study  
22 employed the Regional Earth System Model (RegESM), an online-coupled climate–chemistry–  
23 ecosystem modeling framework, to quantify the impacts of aerosols, surface ozone (O<sub>3</sub>), and  
24 nitrogen deposition on China's net ecosystem productivity (NEP) from 2010 to 2020. The re-  
25 sults show that aerosols enhanced China's NEP by 17.93 TgC yr<sup>-1</sup> (4.49% of the total NEP),  
26 primarily by increasing diffuse radiation, with the most pronounced effects in Southern and  
27 Eastern China. Nitrogen deposition further increased NEP by 37.98 TgC yr<sup>-1</sup> (9.52%),

28 concentrated in Central and Southern regions. In contrast, O<sub>3</sub> pollution reduced NEP by 51.33  
29 TgC yr<sup>-1</sup> (12.90%), particularly in the forest-dominated Southeast. The positive impacts of aer-  
30 osols and nitrogen deposition on the carbon sink weakened over time, whereas the negative  
31 influence of O<sub>3</sub> was increasing. The combined effects indicate that CAA-induced atmospheric  
32 chemistry changes led to a shift in the dominant atmospheric drivers of China's terrestrial car-  
33 bon sink, from enhancement by aerosols and nitrogen deposition to suppression by ozone. Our  
34 findings highlight the need for stronger O<sub>3</sub> pollution control to achieve co-benefits between air-  
35 quality improvement and carbon neutrality.

删除了: reversed the dominant atmospheric drivers

## 36 1 Introduction

37 Terrestrial ecosystems act as major carbon sinks, sequestering atmospheric carbon dioxide  
38 (CO<sub>2</sub>) through plant photosynthesis, and constitute a fundamental natural process for mitigating  
39 global climate change (Friedlingstein et al., 2023; Piao et al., 2013; Yuan et al., 2025). Under  
40 ongoing global warming, the dynamics of carbon sinks are regulated not only by climatic fac-  
41 tors such as temperature and precipitation (Cao et al., 2023; Post et al., 2018; Ren et al., 2020),  
42 but also by variations in atmospheric composition (Zhou et al., 2021). Among these, aerosols,  
43 O<sub>3</sub>, and atmospheric nitrogen deposition have been identified as key atmospheric pollutants  
44 affecting terrestrial carbon sequestration (Liu et al., 2022; Zhou et al., 2024). As a crucial com-  
45 ponent of the global carbon cycle, terrestrial ecosystems in China sequester approximately  
46 0.20–0.25 PgC yr<sup>-1</sup>, playing an essential role in supporting the achievement of the national car-  
47 bon neutrality target (Piao et al., 2022; Xia et al., 2025; Yue et al., 2021). Therefore, assessing  
48 the responses of carbon sinks to multiple atmospheric composition changes is of great scientific  
49 significance for understanding both the global carbon cycle and climate feedback mechanisms.

50 Aerosols influence vegetation photosynthesis and carbon sequestration primarily through  
51 radiative forcing (Shu et al., 2022; Zhou et al., 2022). Aerosol scattering and absorption reduce  
52 surface solar radiation and can suppress vegetation photosynthesis (Doughty et al., 2010;  
53 Kuniyal and Guleria, 2019). In the meantime, enhanced diffuse radiation increases light use  
54 efficiency of plants, leading to the diffuse fertilization effect (Gu et al., 2003; Mercado et al.,  
55 2009). Aerosols also influence cloud microphysics by modifying droplet formation and lifetime,

57 which further affects regional precipitation and water availability for vegetation (Li et al., 2020;  
58 Unger et al., 2017). Consequently, the net effect of aerosols on photosynthesis exhibits marked  
59 spatial heterogeneity, with both enhancement and suppression reported in highly polluted re-  
60 gions such as eastern China (Strada and Unger, 2016; Wang et al., 2018; Xie et al., 2020).

61 In addition, near-surface O<sub>3</sub> impairs plant carbon uptake through direct physiological  
62 damage (Lei et al., 2022; Unger et al., 2020). O<sub>3</sub> enters leaves through stomata and induces  
63 reactive oxygen species at the cellular level, leading to degradation of photosynthetic pigments,  
64 suppressed Rubisco activity, premature leaf senescence, and defoliation, all of which inhibit  
65 photosynthetic carbon assimilation (Wittig et al., 2007). Evidence from O<sub>3</sub>-FACE (free-air O<sub>3</sub>  
66 concentration enrichment) experiments shows that a 10 ppb increase in O<sub>3</sub> concentration can  
67 lower crop productivity by 5–15% (Feng et al., 2015). In China, summertime O<sub>3</sub> peaks often  
68 coincide with the peak growing season of vegetation, particularly in the North China Plain and  
69 the Yangtze River Delta, posing a notable threat to regional carbon sequestration (Lei et al.,  
70 2022; Li et al., 2024; Yue et al., 2017).

71 Furthermore, atmospheric nitrogen deposition is a major external nitrogen source for ter-  
72 restrial ecosystems and exerts both positive and negative effects on carbon sinks (Chen et al.,  
73 2015; Lu et al., 2021). In nitrogen-limited systems, such as temperate forests and grasslands,  
74 moderate deposition can enhance photosynthesis and biomass accumulation, thereby increas-  
75 ing carbon sequestration (Cen et al., 2025; Lu et al., 2016; Peng et al., 2025). When inputs  
76 become excessive, however, they can induce soil acidification, biodiversity loss, and broader  
77 ecosystem degradation, a condition known as nitrogen saturation (Chen et al., 2015; Yue et al.,  
78 2016). China receives some of the highest nitrogen deposition levels globally, with annual av-  
79 erages of 15–20 kg N ha<sup>-1</sup> yr<sup>-1</sup> and hotspots surpassing 30 kg N ha<sup>-1</sup> yr<sup>-1</sup>, raising increasing  
80 concerns about long-term ecological impacts (Liu et al., 2022; Liu et al., 2013; Yu et al., 2019).

81 China has long faced the dual pressures of severe air pollution and growing greenhouse  
82 gas emissions (Tu et al., 2019; Wang et al., 2024). Rapid economic expansion in the early 2010s  
83 was accompanied by persistent increases in fine particulate matter (PM<sub>2.5</sub>) concentrations (Hao  
84 et al., 2020). Since 2013, successive Clean Air Action Plans have led to a substantial decline in  
85 PM<sub>2.5</sub> levels (Xue et al., 2019; Yue et al., 2020; Zheng et al., 2018). At the same time, near-

86 surface summertime O<sub>3</sub> has risen sharply (Liu et al., 2018; Zhou et al., 2024), while nitrogen  
87 deposition has slowed in growth but remains at a high level (Liu et al., 2024). These changes  
88 not only reflect the outcomes of emission control policies but also reshape the regional atmos-  
89 pheric chemical environment, potentially exerting complex and combined effects on carbon  
90 sinks (Liu et al., 2022; Zhou et al., 2024). The rapid transition in atmospheric composition  
91 during 2010–2020 provides an unprecedented large-scale natural experiment for disentangling  
92 the relative roles of aerosols, O<sub>3</sub>, and nitrogen deposition in altering China’s carbon sink. How-  
93 ever, most existing studies have examined these drivers in isolation, relied on offline or statis-  
94 tical frameworks that cannot capture dynamic climate–chemistry–ecosystem feedbacks, and  
95 rarely compared responses across ecological regions (Unger et al., 2020; Yue et al., 2017; Zhou  
96 et al., 2024).

97 Here, we employ an improved regional climate–chemistry–ecosystem online-coupling  
98 model, RegESM (Xie et al., 2024; Zhang et al., 2025), to quantify the impacts of aerosols, O<sub>3</sub>,  
99 and nitrogen deposition on China’s terrestrial carbon sinks during 2010–2020. RegESM incor-  
100 porates two-way interactions among climate, atmospheric chemistry, and biogeochemical pro-  
101 cesses and has been extensively evaluated over East Asia (Ma et al., 2023; Xie et al., 2024; Xie  
102 et al., 2020; Zhang et al., 2025). Our objective is to isolate the contributions of individual at-  
103 mospheric components to changes in China’s carbon sinks based on RegESM after its assess-  
104 ment using multiple observational datasets. These results offer new insight into the ecological  
105 consequences of rapid atmospheric composition changes and provide a scientific foundation  
106 for coordinated multi-pollutant control and ecosystem management under China’s carbon-neu-  
107 trality goals.

## 108 **2 Data and Methods**

### 109 **2.1 The RegESM model**

110 In this study, we employed the RegESM, an improved extension of the RegCM-Chem-  
111 YIBs regional climate–chemistry–ecosystem modeling framework (Xie et al., 2024; Xie et al.,  
112 2019; Zhang et al., 2025). The original RegCM-Chem-YIBs couples the RegCM4 regional

113 climate model (Giorgi et al., 2012), the radiative interactive gas-phase chemistry module Chem  
114 (Shalaby et al., 2012), and the YIBs terrestrial ecosystem model (Yue and Unger, 2015) to  
115 represent interactive processes among atmospheric dynamics, chemistry, and terrestrial carbon  
116 cycles (Xie et al., 2024). Building upon this foundation, RegESM strengthens two-way feed-  
117 back among the atmosphere, atmospheric chemistry, and land surface processes, enabling a  
118 more realistic simulation of biogeochemical cycles (Zhang et al., 2025). The enhanced coupling  
119 allows land surface changes, such as vegetation dynamics and soil moisture variations, to more  
120 directly influence atmospheric composition, radiation, and meteorology, while atmospheric  
121 and chemical variations simultaneously affect ecosystem processes (Xie et al., 2024; Zhang et  
122 al., 2025). This bidirectional integration improves the model's capability to capture transient  
123 and spatially heterogeneous climate–ecosystem–chemistry interactions, which are crucial for  
124 regional climate change and carbon budget assessments (Zhang et al., 2025).

125 The RegESM framework used in this study integrates RegCM4 as the dynamical core for  
126 simulating regional climate processes at a high resolution, the Chem module for interactive  
127 gas-phase and aerosol chemistry coupled with radiation and meteorology, and the YIBs land  
128 surface model for calculating biophysical processes such as photosynthesis, transpiration, and  
129 energy balance, along with biogeochemical cycles of carbon and nitrogen (Giorgi et al., 2012;  
130 Shalaby et al., 2012; Xie et al., 2024; Yue and Unger, 2015). In RegESM, the influence of  
131 atmospheric nitrogen deposition on terrestrial carbon fluxes is represented through the online  
132 coupling between the chemistry and land components. Atmospheric nitrogen deposition is cal-  
133 culated online by the chemistry component as dry and wet deposition fluxes of reduced and  
134 oxidized nitrogen (NH<sub>x</sub> and NO<sub>y</sub>), which are then passed to the land component as external  
135 nitrogen inputs. These inputs affect soil inorganic nitrogen availability and subsequently influ-  
136 ence plant productivity, ecosystem respiration, and net ecosystem productivity. Therefore, the  
137 effect of nitrogen deposition on carbon fluxes is represented as the integrated result of nitrogen  
138 input and land biogeochemical processes, rather than as a simple linear fertilization effect.  
139 These components are linked through an improved coupling mechanism that ensures the con-  
140 sistent exchange of meteorological, chemical, and biogeophysical variables at each model  
141 timestep, enabling fully interactive simulations in which land, atmosphere, and chemistry

142 evolve in a physically coherent manner (Xie et al., 2024; Zhang et al., 2025). This model has  
 143 been widely applied in East Asia (Xie et al., 2025; Xie et al., 2019; Zhang et al., 2025; Zhang  
 144 et al., 2024).

145 We used net ecosystem productivity (NEP) as an indicator for characterizing carbon  
 146 sources and sinks (NEP > 0 suggests a carbon sink). NEP was calculated as the difference  
 147 between gross primary production (GPP) and the sum of autotrophic respiration (Ra) and het-  
 148 erotrophic respiration (Rh) (Xie et al., 2025; Yue et al., 2021). It is noteworthy that the NEP  
 149 estimated in this study does not account for lateral carbon transfers.

## 150 2.2 Ozone Damage Scheme

151 Once surface O<sub>3</sub> enters plants through the stomata, it directly damages plant cellular struc-  
 152 tures and suppresses the photosynthetic rate, thereby reducing vegetation productivity. In the  
 153 YIBs vegetation module of the RegESM model, a semi-mechanistic parameterization scheme  
 154 is employed to represent the impacts of O<sub>3</sub> on plants (Sitch et al., 2007; Yue and Unger, 2015):

$$155 \quad B = B_{tot} \cdot K, \quad (1)$$

156 where B denotes the photosynthetic rate under O<sub>3</sub> exposure,  $B_{tot}$  represents the total leaf pho-  
 157 tosynthetic rate, and K is the remaining proportion of photosynthetic capacity after O<sub>3</sub> stress.  
 158 This proportion is determined by the stomatal O<sub>3</sub> flux that exceeds a specified threshold:

$$159 \quad K = 1 - b \cdot \max[(K_{ozn} - K_{ozncrit}), 0], \quad (2)$$

160 where b denotes the vegetation sensitivity parameter to O<sub>3</sub> derived from observational data.  
 161  $K_{ozncrit}$  represents the threshold of O<sub>3</sub>-induced damage to vegetation, and  $K_{ozn}$  denotes the  
 162 O<sub>3</sub> flux entering the leaf through stomata:

$$163 \quad K_{ozn} = \frac{[O_3]}{r_b + \frac{\kappa_{O_3}}{r_s}}, \quad (3)$$

164 where [O<sub>3</sub>] denotes the O<sub>3</sub> concentration at the canopy top,  $r_b$  is the boundary layer resistance,  
 165  $\kappa_{O_3}$  is the ratio of O<sub>3</sub> leaf resistance to water vapor blade resistance, and  $r_s$  is the stomatal  
 166 resistance accounting for the effects of O<sub>3</sub>:

$$167 \quad r_s = g_s \cdot K. \quad (4)$$

168  $g_s$  denotes the leaf conductance unaffected by O<sub>3</sub> exposure. By simultaneously solving

169 Equations (2), (3), and (4), a quadratic term with respect to  $K$  is obtained, which can be solved  
 170 analytically.

### 171 2.3 Experimental design and input data

172 The simulation domain covers most of East Asia (Fig. S1), centered at 36° N and 107° E.  
 173 The horizontal resolution is 30 km, with 18 vertical layers. To quantify the independent con-  
 174 tributions of aerosol, O<sub>3</sub> damage, and atmospheric nitrogen deposition to China’s terrestrial  
 175 carbon sink during 2010–2020, four sensitivity experiments were conducted (Table 1): a base-  
 176 line simulation without these effects (Base), and three single-factor cases that enabled only  
 177 aerosol (Ctrl\_AOD), O<sub>3</sub>-induced vegetation damage (Ctrl\_O<sub>3</sub>), and nitrogen deposition im-  
 178 pacts (Ctrl\_Ndep). In the Ctrl\_AOD experiment, aerosols were fully coupled to meteorology,  
 179 so that the direct aerosol radiative effect and the associated meteorological responses were  
 180 represented in the simulations, while aerosol indirect effects through cloud processes were not  
 181 included. The difference between each sensitivity case and the Base run represents the corre-  
 182 sponding individual effect. All simulations were preceded by a one-year spin-up to reduce the  
 183 influence of initial conditions. To further assess regional responses, China was divided into six  
 184 representative subregions (Fig. S2), and statistical analyses were performed for each.

185  
 186 **Table 1.** Numerical model experiments.

Simulations	Periods	Aerosol <u>direct</u> radiative effect	O <sub>3</sub> damage	<u>Atmospheric</u> nitrogen deposition
Base	2010-2020	off	off	off
Ctrl_AOD	2010-2020	<u>on</u>	off	off
Ctrl_O <sub>3</sub>	2010-2020	off	<u>on</u>	off
Ctrl_Ndep	2010-2020	off	off	<u>on</u>

删除了: atmospheric

删除了: open

删除了: open

删除了: open

187  
 188 The initial and boundary meteorological fields were taken from the ECMWF (European  
 189 Centre for Medium-Range Weather Forecasts) ERA-Interim reanalysis with a temporal

194 resolution of 6 h and a horizontal resolution of  $1.5^\circ \times 1.5^\circ$  (Hersbach et al., 2020). Aerosol  
195 initial and boundary conditions were provided by the global chemical transport model (MO-  
196 ZART) (Emmons et al., 2010; Horowitz et al., 2003). Background CO<sub>2</sub> fields were constrained  
197 by three-dimensional concentrations from NOAA CarbonTracker (CT) reanalysis (Peters et al.,  
198 2007). The initial parameters for the YIBs model were derived from soil carbon stocks based  
199 on equilibrium tree height and a 30-year harvest cycle (Yue and Unger, 2015). Vegetation  
200 cover was prescribed from MODIS and AVHRR (Advanced Very High Resolution Radiometer)  
201 datasets (Lawrence and Chase, 2007). Anthropogenic emissions in China were taken from the  
202 Multi-resolution Emission Inventory for China (MEIC) (Geng et al., 2024; Li et al., 2017;  
203 Zheng et al., 2018).

#### 204 **2.4 Validation data**

205 We employed monthly mean aerosol optical depth (AOD) data from the MODIS sensor  
206 onboard NASA's Terra satellite (MOD08\_M3.061). The data have a spatial resolution of  $1^\circ \times$   
207  $1^\circ$  and are retrieved using three algorithms: the Dark Target, Deep Blue, and combined ap-  
208 proaches (Levy et al., 2013). Ground-level O<sub>3</sub> observations were obtained from 366 monitoring  
209 stations operated by the China National Environmental Monitoring Center (CNEMC). To eval-  
210 uate the model's capability in simulating atmospheric nitrogen deposition, we employed pub-  
211 licly available datasets (Liu et al., 2024; Zhu et al., 2025). These datasets integrate observations  
212 with model outputs to provide nitrogen deposition estimates at both global and regional scales  
213 over China. To assess the reliability of simulated CO<sub>2</sub>, we used observations from the World  
214 Data Centre for Greenhouse Gases (WDCGG). This dataset provides measured surface atmos-  
215 pheric CO<sub>2</sub> concentrations and was used to evaluate the model's ability to reproduce observed  
216 CO<sub>2</sub> levels. For the spatial distribution of CO<sub>2</sub>, we additionally used CO<sub>2</sub> concentration fields  
217 from CT (Peters et al., 2007). For GPP and net primary production (NPP) validation, we used  
218 the global MODIS products MOD17A2H and MOD17A3H (Collection 6). The GPP data, at  
219 8-day resolution, were derived using the radiation use efficiency algorithm, while NPP  
220 (NPP=GPP-Ra) data were produced by annually accumulating GPP values, with a spatial res-  
221 olution of 500 m (He et al., 2018; Madani et al., 2014).

## 222 2.5 Analytical Approach

223 Aerosol-induced meteorological changes are highly interdependent, making it challenging  
224 to isolate their individual effects on terrestrial carbon cycling. To quantify the relative contri-  
225 butions of these meteorological responses to vegetation carbon fluxes, we applied a multiple  
226 linear regression framework. Standardized regression coefficients were used to assess the rela-  
227 tive influence of each climate variable. This approach has been widely demonstrated as effec-  
228 tive for disentangling the impacts of multiple environmental drivers on ecosystem processes  
229 (Jung et al., 2017; Xie et al., 2025; Zhang et al., 2024).

230 The regression model is expressed as follows:

$$231 \quad \Delta Y = A_1 \times \Delta X_1^{RadD} + A_2 \times \Delta X_2^{RadF} + A_3 \times \Delta X_3^{Temp} + A_4 \times \Delta X_4^{Precip} + A_5 \times \Delta X_5^{VPD} \\ 232 \quad \quad \quad + \varepsilon \quad (5)$$

233 where  $\Delta Y$  denotes the difference in terrestrial carbon flux between the simulations Base and  
234 Ctrl\_AOD, respectively.  $\Delta X_1^{RadD}$ ,  $\Delta X_2^{RadF}$ ,  $\Delta X_3^{Temp}$ ,  $\Delta X_4^{Precip}$  and  $\Delta X_5^{VPD}$  denote  
235 the differences in direct radiation, diffuse radiation, temperature, precipitation, and vapor pres-  
236 sure deficit (VPD) between the simulations Base and Ctrl\_AOD, respectively.  $A_i$  represents  
237 the partial regression coefficient for different meteorological factors, indicating the sensitivity  
238 of carbon flux to variations in these factors.  $\varepsilon$  is the residual term of the regression model. We  
239 use the following equation to calculate the standardized regression coefficient  $B_i$  for compar-  
240 ing the relative impacts of different meteorological factors:

$$241 \quad B_i = A_i \times SD(\Delta X_i) \div SD(\Delta Y) \quad (6)$$

242 where  $SD(\Delta X_i)$  and  $SD(\Delta Y)$  represent the standard deviations of the changes in each mete-  
243 orological factor and carbon flux, respectively.  $B_i$  quantifies the relative contribution of dif-  
244 ferent meteorological factors to variations in carbon flux. This approach enables a quantitative  
245 assessment of the individual impacts of changes in each meteorological factor induced by aer-  
246 osol radiative effects on terrestrial carbon flux.

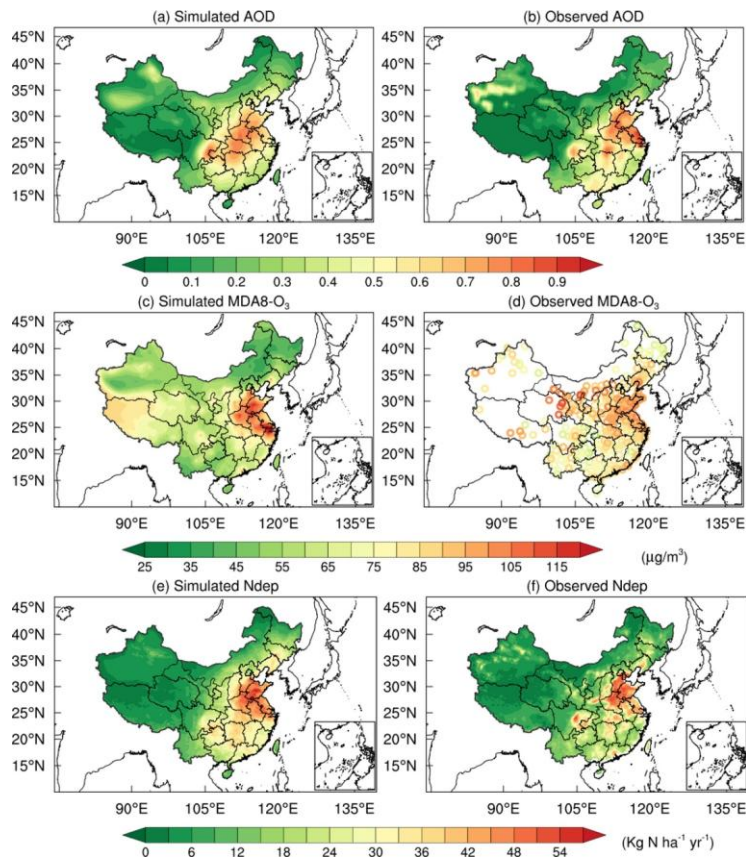
## 247 3 Results

### 248 3.1 Model validations

249 **3.1.1 Aerosols, surface ozone, and atmospheric nitrogen deposition**

250 We assessed the RegESM performance by comparing the 2010–2020 simulations with  
251 multi-source observations. Simulated AOD showed good agreement with MODIS products in  
252 both spatial distribution and magnitude (Fig. 1a, b). High AOD values are located over the  
253 North China Plain and the Sichuan Basin, consistent with dense anthropogenic emissions in  
254 these regions (Luo et al., 2014). The observations indicate that the national mean AOD de-  
255 creased from 0.36 in 2010 to 0.28 in 2020, driven by air quality improvement policies. We  
256 calculated statistical metrics, including the correlation coefficient (R), mean bias (MB), and  
257 root mean square error (RMSE), to evaluate the model performance (Fig. S3). The RegESM  
258 captures this trend with a correlation coefficient (R) of 0.71. However, compared with monthly  
259 MODIS AOD, the model shows a minor underestimation (MB = -0.02), which can be at-  
260 tributed primarily to uncertainties in the anthropogenic emission inventories (Xie et al., 2020).  
261 Surface O<sub>3</sub> simulations reproduce both spatial patterns (Fig. 1c, d). The correlation with site  
262 observations reaches 0.72 (Fig. S4). High concentrations in the North China Plain, the Yangtze  
263 River Delta, and the Sichuan Basin are captured well, highlighting the model’s skill in simu-  
264 lating O<sub>3</sub> fields. The simulated annual mean atmospheric nitrogen deposition flux ranges from  
265 20 to 40 kg N ha<sup>-1</sup> yr<sup>-1</sup> in eastern agricultural and urban areas, consistent with reported values  
266 of 25–35 kg N ha<sup>-1</sup> yr<sup>-1</sup> (Fig. 1e, f). The simulated national mean of 15.09 kg N ha<sup>-1</sup> yr<sup>-1</sup> is close  
267 to the dataset range of 13.45–15.39 kg N ha<sup>-1</sup> yr<sup>-1</sup>. The model also reproduces the observed  
268 decline after the implementation of air pollution control policies in 2013, with a gradual de-  
269 crease after 2015 (Fig. S5). These evaluations indicate that RegESM reliably simulates AOD,  
270 O<sub>3</sub>, and nitrogen deposition fields across China.

271



272

273 **Figure 1.** Annual mean AOD (a, b), maximum daily 8 h average (MDA8) O<sub>3</sub> (c, d), and At-  
 274 mospheric nitrogen deposition (e, f) from model simulation (a, c, e) and observations (b, d, f).

275

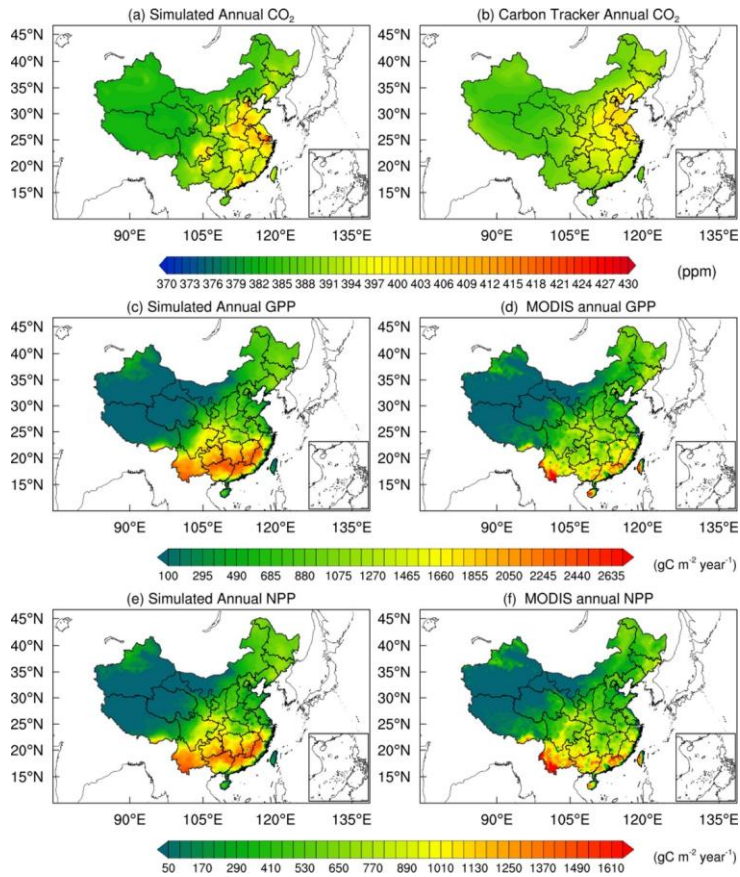
### 276 3.1.2 Atmospheric CO<sub>2</sub> concentrations, GPP, and NPP

277 Simulated CO<sub>2</sub> concentrations were compared with six stations from the WDCGG. The  
 278 correlation coefficients range from 0.83 to 0.96 (Table S1). The YON site shows the best agree-  
 279 ment ( $R = 0.96$ ,  $MB = -1.10$  ppm), likely due to minimal influence from terrestrial emissions.  
 280 In contrast, HKG and HKO show larger biases, with overestimates of 3.1 ppm ( $R = 0.83$ ) and  
 281 3.3 ppm ( $R = 0.84$ ), probably linked to unaccounted variability in urban sources in monthly

282 inventories. Nevertheless, the seasonal cycle is reproduced well at all sites (Fig. S6).

283 We further compared simulated CO<sub>2</sub> with the CarbonTracker CT2022 assimilation dataset  
284 (Peters et al., 2007). The spatial correlation coefficient reaches 0.72 (Fig. 2a, b). High CO<sub>2</sub>  
285 concentrations appear over the Beijing–Tianjin–Hebei region, the Yangtze River Delta, the  
286 Pearl River Delta, and the Sichuan Basin, consistent with intense industrial emissions. The  
287 model slightly overestimates values in the Pearl River Delta, likely due to underrepresented  
288 local sources and complex topography. Overall, RegESM effectively captures the spatial dis-  
289 tribution of CO<sub>2</sub> concentrations.

290 Simulated GPP agrees well with MODIS in spatial distribution (Fig. 2c, d), with a spatial  
291 correlation of 0.89. However, GPP from this study is larger than MODIS GPP by 7.4%, with  
292 largest differences in Central (11.6%) and Southeast China (5.7%). Other studies also found  
293 that MODIS GPP was underestimated at high values (Xie et al., 2019; Zhang et al., 2012). The  
294 southeast-to-northwest decreasing gradient is reproduced, with high values over regions dom-  
295 inated by forest ecosystems. The seasonal cycle of GPP is also captured (Fig. S7). The simu-  
296 lated NPP exhibits a spatial distribution consistent with the MODIS (Fig. 2e, f), with a spatial  
297 correlation coefficient of 0.86. Similar to GPP, the model overestimates NPP by 8.4%, mainly  
298 due to the overestimation in Central (14.3%) and Northeastern (6.2%) China. These results  
299 confirm the model’s ability to represent terrestrial carbon fluxes.



300  
 301 **Figure 2.** Annual mean CO<sub>2</sub> (a, b), GPP (c, d), and NPP (e, f) from model simulation (a, c, e)  
 302 and observations (b, d, f).

303

### 304 3.2 Impacts of Aerosols on Meteorology and Carbon Sinks

#### 305 3.2.1 Impacts of Aerosols on Meteorological Factors

306 During 2010–2020, the aerosol exerted a substantial influence on China’s surface radia-  
 307 tion and near-surface climate (Fig. 3). Nationally, aerosol scattering reduced downward direct  
 308 solar radiation by 8.81 W m<sup>-2</sup> and increased its diffuse component by 3.04 W m<sup>-2</sup>, resulting in  
 309 a net decrease of 5.77 W m<sup>-2</sup> in total downward shortwave radiation at the surface. Spatially,

设置了格式: 上标

设置了格式: 上标

删除了: Nationally, aerosols reduced downward direct solar radiation by 8.81 W m<sup>-2</sup>, while increasing diffuse radiation by 3.04 W m<sup>-2</sup>, leading to an overall reduction of 5.77 W m<sup>-2</sup> in total shortwave radiation reaching the surface.

设置了格式: 上标

314 these radiative changes were most pronounced over major urban agglomerations such as the  
315 North China Plain, the Yangtze River Delta, and the Sichuan Basin, coinciding with regions of  
316 high AOD associated with intensive anthropogenic emissions. These results are consistent with  
317 previous modeling and satellite-based analyses (Wang et al., 2017; Xie et al., 2020), confirming  
318 the robustness of the simulated radiative forcing patterns.

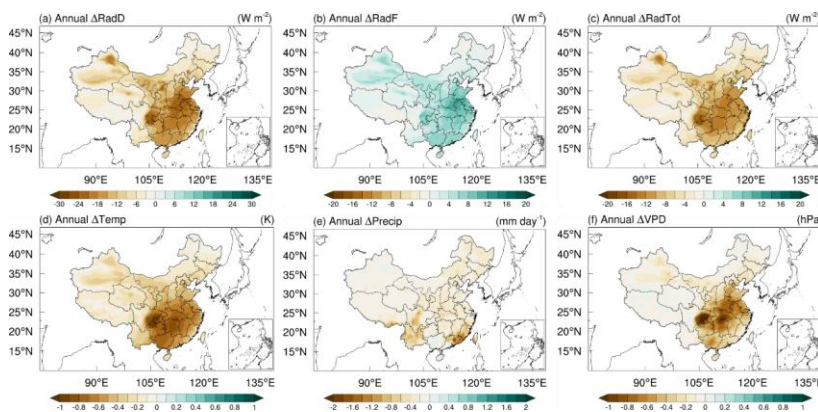
319 The reduction in surface solar radiation directly perturbed the regional energy balance and  
320 atmospheric thermodynamics, resulting in a cooling effect over most of eastern and central  
321 China. As shown in Fig. 3d, surface air temperature decreased significantly in the Sichuan Ba-  
322 sin and coastal regions, with local maxima reaching  $-1.10$  °C. In contrast, western and north-  
323 eastern China experienced weaker changes, consistent with lower AOD levels. The simulated  
324 national mean temperature decline of  $0.32$  °C agrees well with previous RegCM-based studies  
325 (Wang et al., 2015; Xie et al., 2020). This widespread cooling is primarily attributed to aerosol-  
326 induced dimming, which suppresses surface shortwave absorption and weakens boundary-  
327 layer turbulence, thereby inhibiting vertical heat exchange and reducing near-surface tempera-  
328 tures.

329 Aerosol also exerted a marked influence on regional hydrological processes. Precipitation  
330 decreased across much of southern and southwestern China, with notable reductions in Guang-  
331 dong, Fujian, Yunnan, and Sichuan provinces, where daily rainfall decreased by up to  $2$  mm  
332  $\text{day}^{-1}$  (Fig. 3e). On average, national precipitation declined by  $0.23$  mm  $\text{day}^{-1}$ . The reduction in  
333 rainfall reflects the combined effects of radiative cooling and weakened convective activity.  
334 Specifically, aerosol-induced surface dimming stabilizes the lower atmosphere and suppresses  
335 the upward transport of moisture, while reduced latent heating further limits convective cloud  
336 formation. These mechanisms together explain the widespread drying observed in the simula-  
337 tions.

338 The VPD, a key indicator of plant water stress, also responded sensitively to aerosol forc-  
339 ing. As shown in Fig. 3f, aerosols significantly reduced VPD over central and southeastern  
340 China, with decreases of  $-0.30$  to  $-0.60$  hPa, and locally up to  $-1.20$  hPa in Sichuan, Hebei, and  
341 Jiangsu. The national mean reduction was  $-0.11$  hPa. Lower VPD values imply a moister near-  
342 surface environment and weaker atmospheric demand for evapotranspiration. Ecologically, this

343 alleviation of plant water stress can enhance stomatal conductance and facilitate photosynthetic  
 344 carbon uptake, thereby partially compensating for the productivity loss caused by reduced solar  
 345 radiation. Thus, the aerosol-induced decline in VPD represents an important indirect pathway  
 346 through which aerosols modulate the terrestrial carbon cycle, linking atmospheric radiative  
 347 forcing to ecosystem function.

348



349

350 **Figure 3.** Annual mean changes in meteorological variables due to aerosol direct radiative  
 351 effect during 2010–2020. (a) RadD, direct radiation; (b) RadF, diffuse radiation; (c) RadTot,  
 352 total radiation; (d) Temp, air temperature; (e) Precip, precipitation; (f) VPD, vapor pressure  
 353 deficit.

354

### 355 3.2.2 Effects of Aerosols on the Terrestrial Carbon Sink

356 During 2010–2020, the aerosol overall enhanced the productivity of China’s terrestrial  
 357 ecosystems, increasing GPP and NEP by 293.28 TgC yr<sup>-1</sup> and 17.93 TgC yr<sup>-1</sup>, accounting for  
 358 3.98% and 4.49% of the national totals, respectively. Aerosols also increased Rh by 182.44  
 359 TgC yr<sup>-1</sup> over China, indicating that part of the aerosol-induced carbon sink enhancement was  
 360 offset by enhanced soil carbon decomposition. Spatially, the responses of GPP and NEP to the  
 361 aerosol radiative effect displayed significant heterogeneity, with the most pronounced enhance-  
 362 ments occurring in South Central and East (Fig. 4a, b), where GPP increased by 0.32 gC m<sup>-2</sup>  
 363 day<sup>-1</sup> and 0.31 gC m<sup>-2</sup> day<sup>-1</sup>, respectively. These regions are characterized by dense forests and

设置了格式: 上标  
 设置了格式: 上标  
 设置了格式: 上标  
 设置了格式: 上标  
 设置了格式: 上标  
 删除了: with pronounced enhancements in southern and eastern China (Fig. 4a, b). The most significant enhancements occurred in South-Central and East China, where GPP increased by 0.32 gC m<sup>-2</sup> day<sup>-1</sup> and 0.31 gC m<sup>-2</sup> day<sup>-1</sup>, respectively.

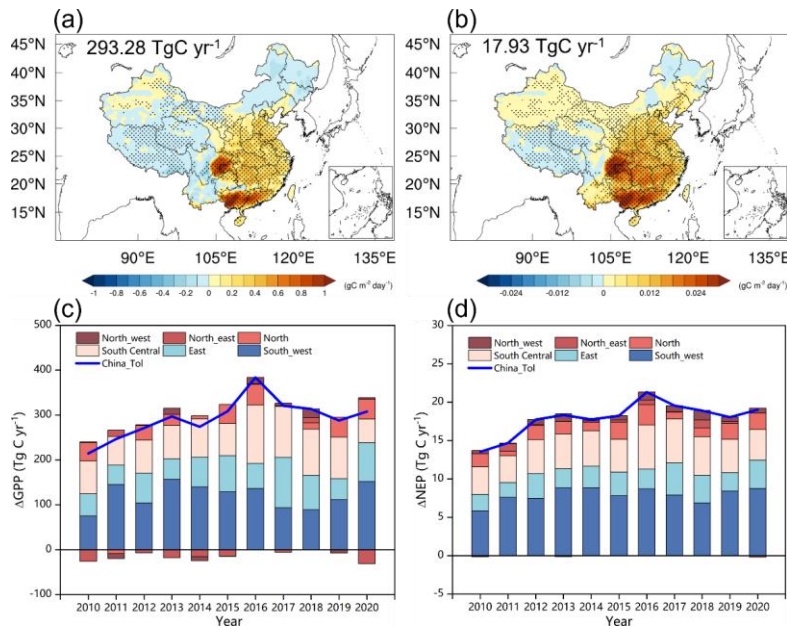
368 cropland ecosystems with high leaf area index, enabling them to fully exploit the additional  
369 diffuse radiation induced by aerosols. Meanwhile, the high aerosol loading in these regions  
370 ensured sufficient radiative perturbation, amplifying the improvement in canopy light-use ef-  
371 ficiency. The spatial pattern of aerosol-induced Rh (Fig. S10a) further shows notable increases  
372 in southern China, broadly consistent with the regions of enhanced ecosystem productivity,  
373 suggesting that greater carbon input to soils likely stimulated microbial decomposition and  
374 partially counteracted the NEP gain. In the Southwest, the response was more complex. Alt-  
375 hough the mean GPP increased by  $0.20 \text{ gC m}^{-2} \text{ day}^{-1}$ , parts of Yunnan showed a negative effect.  
376 This reduction likely results from excessive attenuation of solar radiation under the region's  
377 unique topographic and climatic conditions, which constrained photosynthetic activity. Never-  
378 theless, NEP in this region remained positive (approximately  $0.01 \text{ gC m}^{-2} \text{ day}^{-1}$ ), suggesting  
379 that the cooling effect of aerosols substantially suppressed ecosystem respiration, thereby com-  
380 pensating for the reduced photosynthesis. In contrast, the North and Northwest exhibited weak  
381 positive responses ( $<0.07 \text{ gC m}^{-2} \text{ day}^{-1}$ ), while the Northeast showed slight inhibition ( $-0.04$   
382  $\text{gC m}^{-2} \text{ day}^{-1}$ ), probably due to aerosol-induced cooling delaying the onset of the growing sea-  
383 son. Overall, the spatial patterns of GPP and NEP responses to the aerosol radiative effect show  
384 a clear latitudinal gradient: the humid, high-biomass ecosystems in southern and eastern China  
385 are most sensitive to diffuse radiation enhancement, whereas the high-latitude and arid regions  
386 experience limited or even negative responses due to temperature and radiation constraints.

387 From 2010 to 2020, the influence of aerosols on carbon fluxes exhibited distinct interan-  
388 nual variability (Fig. 4c, d). Both GPP and NEP showed an upward trend before 2016, with  
389 GPP increasing from  $214.66 \text{ TgC yr}^{-1}$  in 2010 to  $384.00 \text{ TgC yr}^{-1}$  in 2016, and NEP rising from  
390  $13.54 \text{ TgC yr}^{-1}$  to  $21.31 \text{ TgC yr}^{-1}$ . The synchronous growth of GPP and NEP indicates that the  
391 aerosol radiative effect enhanced terrestrial carbon uptake mainly through photosynthetic ac-  
392 tivity. The strong enhancement during 2015–2017 coincided with years of high aerosol loading  
393 and a greater proportion of diffuse radiation, which improved canopy light-use efficiency under  
394 humid and cloudy conditions. After 2018, the positive effect weakened slightly and stabilized  
395 at a lower level. This reduction likely reflects the combined influence of cleaner atmospheric  
396 conditions and changing meteorological patterns, including increased direct radiation and a

397 reduced diffuse fraction. Year-to-year variations were further modulated by hydroclimatic con-  
398 ditions: higher humidity and cloud cover enhanced aerosol scattering efficiency, while drier or  
399 cleaner years favored direct radiation and weakened the diffuse light advantage. Moreover, the  
400 smaller NEP fluctuations compared to GPP imply a delayed response of ecosystem respiration,  
401 as aerosol-induced cooling moderates' respiration more gradually than photosynthesis. Overall,  
402 the interannual variability of GPP and NEP responses to the aerosol radiative effect highlights  
403 the coupled influences of aerosol loading, radiation balance, and regional climate variability  
404 on China's terrestrial carbon sink dynamics.

405 The effects of aerosols on GPP and NEP show pronounced seasonal variation (Fig. S8),  
406 driven by the dynamic coupling between vegetation phenology and environmental factors. In  
407 spring (March–May), aerosols increase GPP by 42.35 TgC (14.4%) and NEP by 2.82 TgC  
408 (15.7%), making a notable contribution at the start of the growing season as rising temperatures  
409 and rapid canopy expansion enhance diffuse radiation benefits, improving light-use efficiency;  
410 meanwhile, moderate cooling suppresses respiration without causing thermal stress, further  
411 boosting NEP. In summer (June–August), positive effects peak, with GPP rising by 173.62 TgC  
412 (59.2%) and NEP by 10.15 TgC (56.6%); under high solar radiation and full canopy closure,  
413 diffuse light penetration reaches its maximum, while cooling alleviates heat stress and reduces  
414 respiration, driving NEP to its annual maximum. In autumn (September–November), aerosols  
415 add 88.38 TgC to GPP (30.1%) and 3.95 TgC to NEP (22.0%), effectively extending the pho-  
416 tosynthetic period as shorter days and reduced total radiation increase the proportion of diffuse  
417 light, sustaining carbon storage. In winter (December–February), GPP declines slightly (-  
418 11.07 TgC, -3.8%), but NEP shows a small positive gain (1.01 TgC, 5.6%) because cooling  
419 strongly suppresses respiration, offsetting reduced photosynthesis. Overall, aerosol radiative  
420 effects regulate seasonal carbon cycling by modifying radiation and thermal conditions. The  
421 net impact depends on the trade-off between the fertilization effect of diffuse radiation and the  
422 opposing effects of reduced total radiation and cooling. Summer emerges as the primary driver  
423 of the annual net positive effect. Accurately quantifying this seasonal dynamic is crucial for  
424 assessing the ecological and climatic consequences of anthropogenic aerosols.

425



426  
 427 **Figure 4.** Spatiotemporal variations in carbon flux changes caused by the aerosol radiative  
 428 effect during 2010–2020. (a–b) Multi-year mean spatial patterns of GPP and NEP changes  
 429 caused by the aerosol radiative effect. National totals are shown in each panel. Black dots de-  
 430 note significant changes ( $p < 0.01$ ). (c–d) Interannual variations of GPP and NEP changes  
 431 caused by the aerosol radiative effect.

432

### 433 3.2.3 Contributions of Meteorological Factors to Carbon Sink Changes

434 We quantified the independent contributions of aerosol-induced meteorological changes  
 435 to carbon fluxes using the multiple linear regression analysis described in Section 2.5 (Fig. 5a,  
 436 b). Overall, aerosol substantially influenced China’s terrestrial carbon uptake by altering radi-  
 437 ation composition and meteorological conditions. At the national scale, the increase in diffuse  
 438 radiation emerged as the dominant positive driver, contributing to GPP ( $325.07 \text{ TgC yr}^{-1}$ ) and  
 439 NEP ( $11.46 \text{ TgC yr}^{-1}$ ). This highlights the crucial role of the diffuse radiation fertilization effect,  
 440 particularly in regions with high aerosol loading across eastern and southwestern China, where  
 441 enhanced diffuse light improves canopy light distribution and photosynthetic efficiency. In

442 contrast, the reduction in direct radiation suppressed GPP (94.78 TgC yr<sup>-1</sup>) and NEP (2.59 TgC  
443 yr<sup>-1</sup>) due to insufficient illumination, though the impact on NEP was weaker, reflecting partial  
444 offset by the reduction in ecosystem respiration under aerosol-induced cooling. Cooling alone  
445 reduced GPP by 59.62 TgC yr<sup>-1</sup> and NEP by 4.73 TgC yr<sup>-1</sup>. This decline in NEP occurred  
446 because the decrease in GPP (driven by reduced transpiration and stomatal conductance) out-  
447 weighed the concurrent reduction in ecosystem respiration. Meanwhile, lower VPD enhanced  
448 GPP by 114.44 TgC yr<sup>-1</sup> and NEP by 8.25 TgC yr<sup>-1</sup> by alleviating water stress, reinforcing  
449 photosynthetic carbon uptake. Changes in precipitation played only a minor role, slightly re-  
450 ducing GPP (8.17 TgC yr<sup>-1</sup>) and NEP (0.62 TgC yr<sup>-1</sup>), with limited influence even in the mon-  
451 soon regions of southern China. These findings indicate that variations in radiation components,  
452 rather than hydrometeorological perturbations, serve as the primary pathway through which  
453 aerosols modulate terrestrial carbon sinks.

454 Regionally, among these factors, diffuse radiation exerted the strongest positive influence  
455 on GPP across all regions, particularly in the Southwest (115.92 TgC yr<sup>-1</sup>), East (67.04 TgC yr<sup>-1</sup>),  
456 and South Central (93.08 TgC yr<sup>-1</sup>) China (Fig. 5a, b). Enhanced diffuse light under elevated  
457 aerosol loading improved the vertical distribution of photosynthetically active radiation within  
458 the canopy and increased photosynthetic efficiency. In contrast, direct radiation consistently  
459 exhibited negative effects, most evident in the southwest (-42.32 TgC yr<sup>-1</sup>) and east (-22.92  
460 TgC yr<sup>-1</sup>), indicating that aerosol-induced solar dimming partly offset the diffuse radiation fer-  
461 tilization benefit. Temperature changes associated with aerosol cooling suppressed GPP na-  
462 tionwide, especially in the Southwest (-29.07 TgC yr<sup>-1</sup>) and South Central (-16.19 TgC yr<sup>-1</sup>),  
463 by lowering canopy temperature and reducing evapotranspiration. The contributions of precip-  
464 itation were minor (-1 to -3 TgC yr<sup>-1</sup>), while VPD exerted a positive effect, particularly in  
465 humid Southwest (55.76 TgC yr<sup>-1</sup>), suggesting that aerosol-induced cooling and moistening  
466 alleviated water stress and indirectly promoted carbon uptake. For NEP, diffuse radiation re-  
467 mained the dominant positive driver, with the largest increases in the Southwest (4.06 TgC yr<sup>-1</sup>)  
468 and south-central (3.35 TgC yr<sup>-1</sup>) China, while direct radiation continued to exert negative  
469 effects. The temperature effect was moderate but consistent with GPP, implying that aerosol

删除了: southwest

删除了: east

删除了: south-central

删除了: southwest

删除了: south-central regions

删除了: southern

删除了: regions

删除了: in the southwest

删除了: southwest

479 cooling simultaneously suppressed photosynthesis and respiration, with a net positive outcome  
480 for NEP. Taken together, these spatial contrasts highlight the combined effects of aerosol com-  
481 position, vegetation structure, and regional hydroclimate, emphasizing that radiative forcing  
482 dominates in humid, high-biomass ecosystems, whereas climatic constraints prevail in arid  
483 zones.

484 To further clarify the dominant controls of these spatial differences, we identified the pri-  
485 mary meteorological drivers of GPP and NEP based on the standardized regression coefficients  
486 (Fig. 5c, d, and Table 2). The results indicate that for GPP, diffuse radiation accounts for the  
487 largest proportion (77.83%), followed by vapor pressure deficit (9.27%) and direct radiation  
488 (8.4%), while the influence of temperature (4.45%) and precipitation (0.05%) is relatively  
489 small. For NEP, diffuse radiation remains the dominant driver (72.20%), followed by direct  
490 radiation (15.92%) and temperature (5.64%). These results highlight that aerosols modify the  
491 radiation composition, particularly by enhancing diffuse radiation, which substantially in-  
492 creases photosynthetic efficiency and strengthens the regional carbon sink. In contrast, the ef-  
493 fects of temperature and VPD are weaker overall but more pronounced in northern arid and  
494 semi-arid regions, where water limitation constrains carbon uptake. Collectively, these findings  
495 confirm that radiation composition primarily controls the spatiotemporal dynamics of China's  
496 terrestrial carbon sink, while temperature and moisture factors exert region-dependent modu-  
497 lations.

498

499 **Table 2.** Proportion of dominant meteorological factors for GPP and NEP across China  
500 (Units: %).

Factors	RadD (%)	RadF (%)	Temp (%)	Precip (%)	VPD(%)
GPP	8.40	77.83	4.45	0.05	9.27
NEP	15.92	72.20	5.64	0.14	6.10

501

502

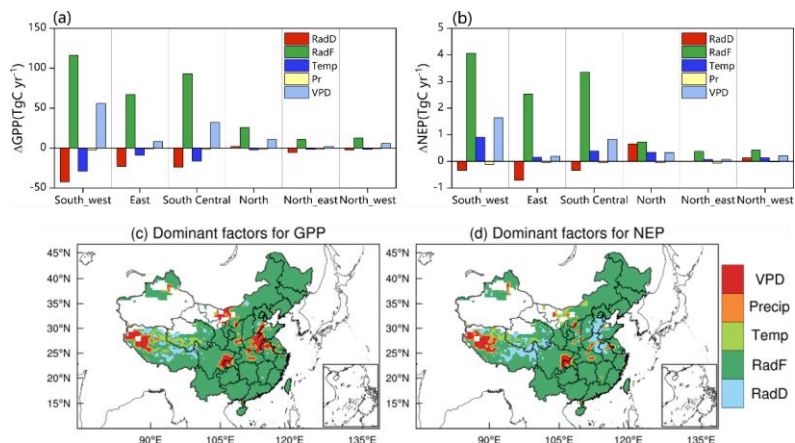
503

504

505

506

507



508

509 **Figure 5.** Effect of aerosol-induced changes in meteorological factors on GPP and NEP, and  
 510 spatial patterns of dominant factors. (a) Regional contributions of individual meteorological  
 511 factors to GPP; (b) Regional contributions of individual meteorological factors to NEP; (c)  
 512 Spatial distribution of the dominant meteorological factor for GPP; (d) Spatial distribution of  
 513 the dominant meteorological factor for NEP.

514

### 515 3.3 Effects of surface ozone on carbon sinks

516 During 2010–2020, surface  $O_3$  in China increased and imposed a persistent suppression  
 517 on terrestrial carbon sinks. Simulations show a strong reduction of GPP by  $0.4\text{--}0.6\ gC\ m^{-2}\ day^{-1}$   
 518 <sup>1</sup> in most regions, with more than  $0.8\ gC\ m^{-2}\ day^{-1}$  in Southeast and Southwest China (Fig. 6a).  
 519 NEP shows a similar spatial pattern (Fig. 6b). The largest decline occurs in the southeast (Yang-  
 520 tze River basin and South China coast), with NEP reduced by  $0.06\text{--}0.08\ gC\ m^{-2}\ day^{-1}$  and  
 521 locally above  $0.1\ gC\ m^{-2}\ day^{-1}$ , consistent with high  $O_3$  and evergreen broadleaf forests (Yue et  
 522 al., 2017). In the southwest (Sichuan Basin and Yunnan–Guizhou Plateau), NEP decreases by  
 523  $0.03\text{--}0.06\ gC\ m^{-2}\ day^{-1}$ , related to complex terrain and dense forests. Impacts are weaker in  
 524 Northeast and Northwest China, mostly below  $0.02\ gC\ m^{-2}\ day^{-1}$ . In Shandong, Henan, and  
 525 northern Jiangsu, the simulated losses are small, reflecting cropland-dominated land cover.

526 However, earlier studies reported strong O<sub>3</sub> effects on crops (Ren et al., 2012), suggesting possible underestimation. This bias may stem from the simplified crop representation in the model (Fig. S2). Nationwide, O<sub>3</sub> reduces GPP and NEP by 749.44 TgC yr<sup>-1</sup> and 51.33 TgC yr<sup>-1</sup>, accounting for 10.17 % and 12.90 % of the totals. O<sub>3</sub> also decreased Rh by 288.17 TgC yr<sup>-1</sup>, with the strongest reductions occurring in eastern and southern China (Fig. S10b). This indicates that the O<sub>3</sub>-induced suppression of ecosystem carbon uptake was partly offset by a concurrent decline in heterotrophic respiration. This pattern suggests that reduced photosynthesis and carbon allocation under O<sub>3</sub> stress decreased litter input and belowground carbon supply, thereby limiting microbial substrate availability and weakening soil carbon decomposition. The suppression is attributed to reduced photosynthesis, altered stomatal conductance, and shifts in carbon allocation, which together weaken ecosystem sinks.

537 The annual effect intensifies until 2018 and then weakens (Fig. 6c). In 2010, O<sub>3</sub> reduces NEP by 42.93 TgC yr<sup>-1</sup>, reaching 55.71 TgC yr<sup>-1</sup> in 2018. It then decreases to 51.98 TgC yr<sup>-1</sup> in 2019 and 51.77 TgC yr<sup>-1</sup> in 2020. These variations reflect air pollution control policies. Between 2013 and 2017, the first Clean Air Action reduced PM<sub>2.5</sub> and NO<sub>x</sub> but left volatile organic compounds (VOCs) largely uncontrolled, thereby enhancing O<sub>3</sub> formation, especially in VOCs-limited regions (Lu et al., 2020). Both model and observations show higher O<sub>3</sub> during this stage (Fig. S4). After 2018, the second Clean Air Action introduced coordinated control of NO<sub>x</sub> and VOCs in the Yangtze River Delta and Pearl River Delta, reducing O<sub>3</sub> during summer and easing sink suppression in 2019–2020. In contrast, O<sub>3</sub> continued to rise in North China, indicating uneven policy outcomes across regions.

547 Seasonal effects are distinct (Fig. 6d and Fig. S9). Summer shows the strongest suppression, with NEP reduced by 29.10 TgC (56.69 % of the annual effect). This results from the overlap of peak O<sub>3</sub> and peak photosynthesis, when high temperature and humidity keep stomata open and allow O<sub>3</sub> uptake. Spring is second, with NEP reduced by 11.67 TgC (22.74 %). The effect is linked to leaf expansion, rapid growth, and frequent transport events. Autumn and winter show weaker impacts due to lower photosynthesis, unfavorable O<sub>3</sub> chemistry, and reduced stomatal conductance. Regional differences are evident: in the south, suppression extends from spring to late autumn, while in the north it is confined to summer. This highlights

设置了格式: 下标

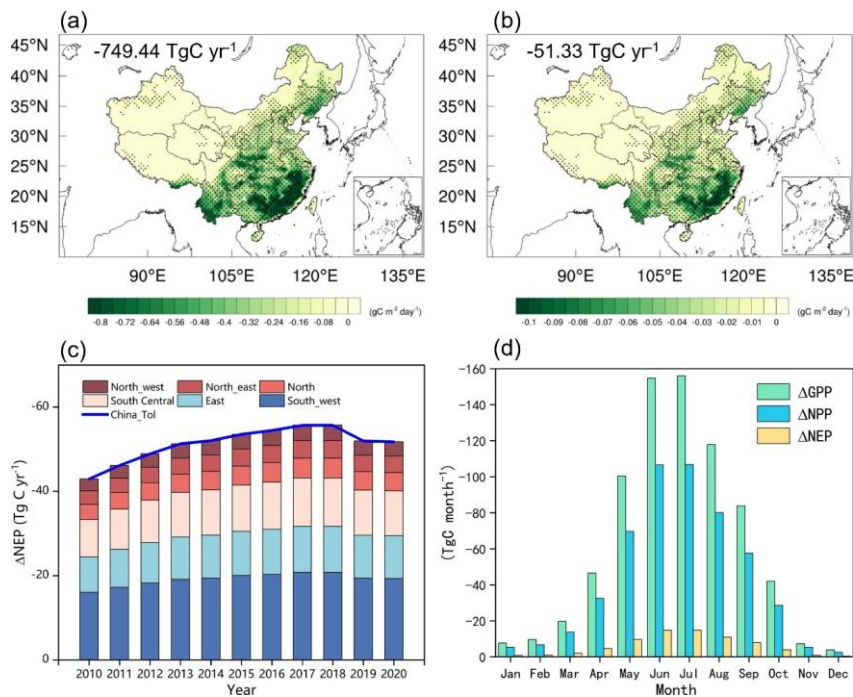
设置了格式: 上标

设置了格式: 下标

设置了格式: 下标

555 the role of climate and phenology in modulating the impact of O<sub>3</sub> on carbon sinks.

556



557

558 **Figure 6.** Spatiotemporal variations in O<sub>3</sub>-induced changes in carbon fluxes during 2010–2020.

559 (a–b) Multi-year mean spatial patterns of O<sub>3</sub>-induced changes in GPP and NEP. National totals

560 are shown in each panel. Black dots denote significant changes ( $p < 0.01$ ). (c) Interannual

561 variation of O<sub>3</sub>-induced NEP. (d) O<sub>3</sub>-induced monthly variations in GPP, NPP, and NEP.

562

### 563 3.4 Effects of atmospheric nitrogen deposition on carbon sinks

564 The response of China's terrestrial ecosystems to atmospheric nitrogen deposition during

565 2010–2020 shows pronounced spatial heterogeneity (Fig. 7a, b). At the national scale, nitrogen

566 deposition increased GPP and NEP by 668.88 TgC yr<sup>-1</sup> and 37.98 TgC yr<sup>-1</sup>, respectively. These

567 increases account for 9.08% of total GPP and 9.52% of total NEP. Atmospheric nitrogen dep-

568 osition also increased Rh by 297.26 TgC yr<sup>-1</sup> over China, indicating that the nitrogen-induced

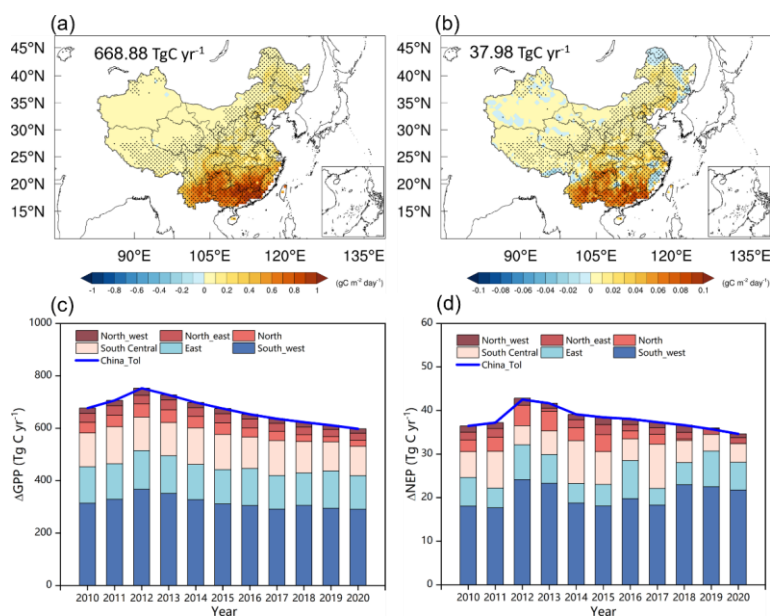
569 enhancement of carbon uptake was accompanied by stronger soil carbon decomposition. The

设置了格式: 上标

570 net gains were mainly concentrated in the southeastern, southwestern, and central regions. In  
571 these areas, NEP increased by 0.04–0.08 g C m<sup>-2</sup> day<sup>-1</sup>, forming the dominant contribution to  
572 the nitrogen-induced carbon sink. Although atmospheric nitrogen deposition is highest in east-  
573 ern China (Fig. 2e, f), the regional variations in GPP and NEP induced by nitrogen deposition  
574 are more pronounced in southern China than in the east. The strong spatial gradient highlights  
575 that the ecological effects of nitrogen deposition are not uniform, but tightly linked to anthro-  
576 pogenic nitrogen emissions and ecosystem sensitivity (Shang et al., 2024). High responses were  
577 observed in regions with intensive agriculture and industry, where deposition exceeded 15 kg  
578 N ha<sup>-1</sup> yr<sup>-1</sup>. Vegetation dominated by subtropical evergreen broadleaf forests, mixed forests,  
579 and croplands is generally nitrogen-limited. Additional nitrogen input alleviated nutrient con-  
580 straints, enhanced photosynthesis and biomass accumulation, and shifted soil microbial pro-  
581 cesses. The spatial pattern of Rh (Fig. S10c) also shows pronounced positive responses in  
582 southern China, consistent with the regions of strong nitrogen-induced carbon uptake. This  
583 suggests that enhanced plant production and carbon input to soils stimulated microbial decom-  
584 position, so that the final NEP gain reflects the balance between increased NPP and increased  
585 Rh rather than a simple linear fertilization effect. When stimulation of GPP and NPP out-  
586 weighed the increase in ER, NEP rose. Warm and humid climates, together with long growing  
587 seasons, further amplified these effects.

588 The impacts of nitrogen deposition on GPP and NEP varied strongly over time (Fig. 7c,  
589 d). In 2010, deposition enhanced NEP by 36.45 TgC yr<sup>-1</sup>. The effect increased to a peak of  
590 42.50 TgC yr<sup>-1</sup> in 2012, but then declined, reaching 34.65 TgC yr<sup>-1</sup> by 2020. This trajectory  
591 reflects the influence of China's air pollution control policies on ecosystem carbon dynamics.  
592 The temporal trend corresponds to changes in nitrogen deposition fluxes. Between 2010 and  
593 2012, rapid industrialization and agriculture raised deposition from 15.85 to 17.91 kg N ha<sup>-1</sup>  
594 yr<sup>-1</sup> (+13%). After 2013, emission reduction policies reduced nitrogen deposition, which fell to  
595 13.25 kg N ha<sup>-1</sup> yr<sup>-1</sup> in 2020 (-26.02%). Notably, the effect of nitrogen deposition on NEP  
596 leveled off after 2015, which can be attributed to the slower decline rate of atmospheric nitro-  
597 gen deposition since 2015 (Fig. S5). The reduction in NEP (-18.47%) was smaller than that in  
598 nitrogen input. This lagged response suggests that soil nitrogen pools accumulated from long-

599 term deposition continued to supply nitrogen to vegetation, buffering the decline.



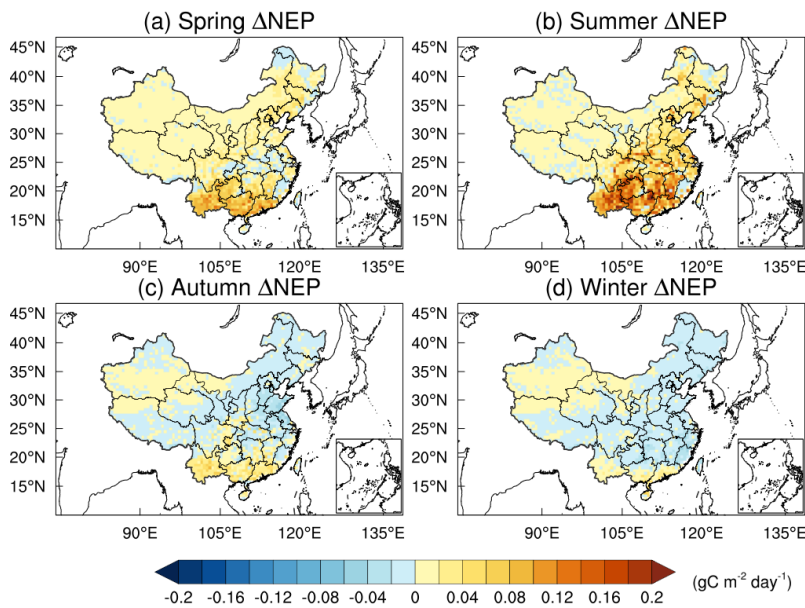
600  
601 **Figure 7.** Spatiotemporal variations in Ndep-induced changes in carbon fluxes during 2010–  
602 2020. (a–b) Multi-year mean spatial patterns of Ndep-induced changes in GPP and NEP. Na-  
603 tional totals are shown in each panel. Black dots denote significant changes ( $p < 0.01$ ). (c-d)  
604 Interannual variation of Ndep-induced in GPP and NEP.

606 The influence of nitrogen deposition on NEP displayed clear seasonality (Fig. 8). Strong  
607 positive effects occurred in summer and spring, whereas autumn and winter showed overall  
608 suppression at the national scale. Summer accounted for the largest gain, with an NEP increase  
609 of 27.16 TgC. Spring followed with 14.12 TgC. In contrast, autumn and winter reduced NEP  
610 by 0.20 and 3.10 TgC, respectively. These seasonal differences result from the combined influ-  
611 ence of multiple factors. During summer, optimal temperature, light, and water supported vig-  
612 orous canopy photosynthesis. Plants assimilated nitrogen efficiently, leading to higher GPP and  
613 biomass accumulation. Spring growth stages were also nitrogen-sensitive, producing strong  
614 positive responses. In autumn and winter, however, plant activity slowed. Nitrogen inputs  
615 mainly stimulated heterotrophic respiration, while GPP and NPP remained low. As a result,

删除了: Strong positive effects occurred in summer and spring, while autumn and winter showed suppression

618 NEP decreased, and carbon sink strength weakened outside the growing season. However, the  
 619 negative response in autumn and winter was not spatially uniform. Positive NEP anomalies  
 620 were still evident in parts of the eastern Qinghai–Tibet Plateau and western Sichuan, especially  
 621 in autumn (Fig. 8c), whereas in winter this signal became much weaker and more localized  
 622 (Fig. 8d). This spatial heterogeneity likely reflects the combined effects of persistent nitrogen  
 623 limitation and weak heterotrophic respiration responses under cold, high-elevation conditions.  
 624 In these regions, low temperatures constrain soil decomposition more strongly, so the stimula-  
 625 tion of heterotrophic respiration by additional nitrogen is limited. Meanwhile, alpine grasslands,  
 626 shrublands, and montane forests may still maintain some residual photosynthetic activity dur-  
 627 ing the late growing season, allowing deposited nitrogen to support carbon uptake. As a result,  
 628 nitrogen deposition can still enhance NEP locally in autumn, even though most other regions  
 629 show seasonal carbon sink weakening.

630



631 **Figure 8.** Spatial distribution of Ndep-induced seasonal variations in NEP during 2010–2020  
 632 (units:  $\text{gC m}^{-2} \text{day}^{-1}$ ). (a) Spring, including March, April, and May. (b) Summer, including June,  
 633 July, and August. (c) Autumn, including September, October, and November. (d) Winter, in-  
 634 cluding January, February, and December.

636

### 637 3.5 Integrated Impact Analysis

638 To assess the combined influence of aerosols, O<sub>3</sub>, and atmospheric nitrogen deposition on  
639 China's terrestrial carbon sink, the three independent effects were algebraically summed. Dur-  
640 ing 2010–2020, the co-evolution of these atmospheric factors jointly drove substantial interan-  
641 nual variability and stage-dependent changes in carbon uptake, closely linked to the implemen-  
642 tation of the CAA plan. The interannual trend (Fig. 9) shows that although aerosols and nitrogen  
643 deposition generally enhanced carbon sequestration, the strong carbon loss caused by O<sub>3</sub>  
644 largely offset these positive effects. The mean net effect was 4.58 TgC yr<sup>-1</sup>, exhibiting pro-  
645 nounced fluctuations and a declining trend. Net enhancement was strong in the early years of  
646 the decade but weakened steadily and approached neutral levels by 2018–2020, when a slight  
647 negative value (-0.14 TgC yr<sup>-1</sup>) first appeared. These changes indicate a gradual transition from  
648 an enhancement-dominated to an inhibition-dominated regime.

649 To further interpret this transition, the study period was divided into three phases accord-  
650 ing to key CAA milestones, and the dominant factors were identified (Fig. 9a). In pre-CAA  
651 (2010–2013), the mean annual net effect reached 8.22 TgC yr<sup>-1</sup>, characterized by nitrogen-  
652 deposition-dominated enhancement. Nitrogen deposition provided the largest positive contri-  
653 bution (+39.47 TgC yr<sup>-1</sup>), while the diffuse-radiation fertilization effect of aerosols offered a  
654 secondary gain (+16.08 TgC yr<sup>-1</sup>). The negative impact of O<sub>3</sub> (-47.33 TgC yr<sup>-1</sup>) was largely  
655 compensated by the two positive drivers, resulting in a pronounced increase in carbon sink  
656 strength. This stage corresponded to relatively high emissions of aerosol and nitrogen precur-  
657 sors, which maintained elevated aerosol loading and nitrogen deposition, while O<sub>3</sub> pollution  
658 had not yet reached the stronger suppressive level observed in later years. During CAA Phase  
659 I (2014–2017), the mean net effect decreased sharply to 3.50 TgC yr<sup>-1</sup>, marking a transitional  
660 stage with competing influences. The positive effect of aerosols peaked (+19.22 TgC yr<sup>-1</sup>),  
661 likely because aerosol changes during this period were more favorable for diffuse-radiation  
662 fertilization, despite the concurrent declines in both scattering and absorbing aerosols. However,  
663 this gain was largely offset by intensified O<sub>3</sub>-induced inhibition (-53.80 TgC yr<sup>-1</sup>). This phase

设置了格式: 下标

删除了: likely due to enhanced scattering as absorbing components were preferentially reduced

666 coincided with strong reductions in emissions of  $\text{SO}_2$ ,  $\text{PM}_{2.5}$  and  $\text{NO}_x$  under the first Clean Air  
667 Action (Fig. S11), which substantially altered atmospheric composition. Although declining  
668 aerosol loading weakened the total radiative perturbation, the remaining aerosol conditions still  
669 supported a strong diffuse-radiation effect. Meanwhile, insufficient VOCs control favored  $\text{O}_3$   
670 formation in many regions, thereby amplifying  $\text{O}_3$ -induced suppression of the carbon sink. In  
671 CAA Phase II (2018–2020), the mean net effect further declined to  $1.19 \text{ TgC yr}^{-1}$ , forming an  
672  $\text{O}_3$ -dominated pattern. This stage was associated with further declines in aerosol concentrations  
673 and nitrogen deposition under continued emission reductions, which weakened their positive  
674 contributions to NEP. At the same time, the coordinated control of  $\text{NO}_x$  and VOCs in key re-  
675 gions partly alleviated  $\text{O}_3$  pollution, but this improvement was not sufficient to reverse the  
676 dominant suppressive role of  $\text{O}_3$  at the national scale. Overall, the stage-dependent changes in  
677 the net carbon sink effect were broadly consistent with the temporal evolution of anthropogenic  
678 emissions during 2010–2020 (Fig. S11), highlighting the strong imprint of CAA-related emis-  
679 sion controls on the balance among aerosols,  $\text{O}_3$ , and nitrogen deposition. With continued emis-  
680 sion control, the aerosol-induced enhancement decreased from its peak ( $+18.66 \text{ TgC yr}^{-1}$ ), and  
681 the nitrogen-deposition gain weakened ( $+35.68 \text{ TgC yr}^{-1}$ ). Although  $\text{O}_3$  suppression slightly  
682 eased ( $-53.15 \text{ TgC yr}^{-1}$ ), it still nearly balanced the combined positive contributions, indicating  
683 a fundamental shift in atmospheric drivers controlling China’s terrestrial carbon sink.

684 The spatial overlay further supports these findings (Fig. 9b, c, d). In forested and indus-  
685 trialized regions of eastern and southern China, the cancellation between positive and negative  
686 effects was most pronounced. These areas, benefiting from nitrogen and aerosol fertilization  
687 but suffering from intense  $\text{O}_3$  pollution, became hotspots of weakened or even reversed net  
688 effects. Overall, the CAA plan not only improved air quality but also altered atmospheric com-  
689 position in ways that substantially affected China’s terrestrial carbon sinks. Policy-driven emis-  
690 sion changes transformed the system from a nitrogen–aerosol-enhanced regime to an  $\text{O}_3$ -dom-  
691 inated offset pattern. These results suggest that achieving synergistic benefits between air-qual-  
692 ity improvement and carbon neutrality requires elevating  $\text{O}_3$  mitigation to a higher strategic  
693 priority.

694

设置了格式: 下标

设置了格式: 下标

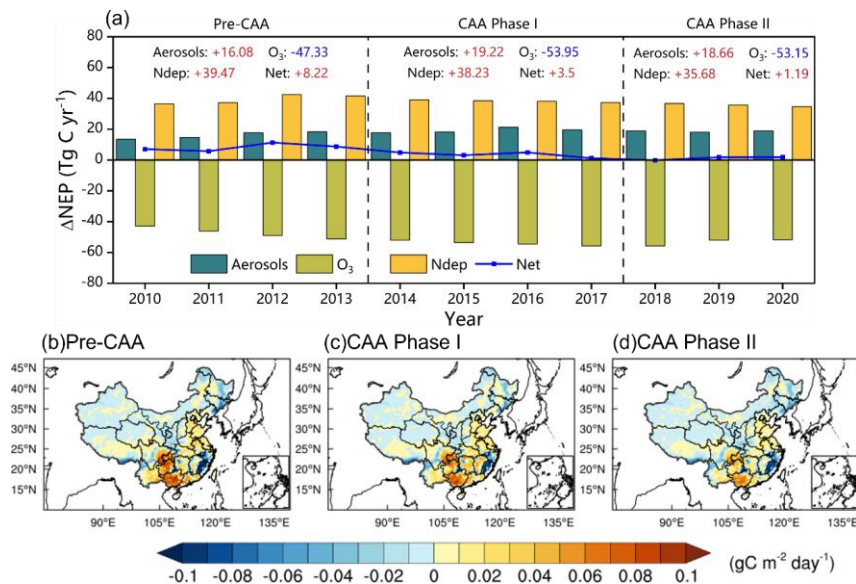
设置了格式: 下标

设置了格式: 下标

设置了格式: 下标

设置了格式: 下标

设置了格式: 下标



695  
 696 **Figure 9.** The overall impacts of aerosols, O<sub>3</sub>, and atmospheric nitrogen deposition on the ter-  
 697 restrial carbon sink in China during 2010–2020. (a) Interannual variations of the combined  
 698 effects. Pre-CAA represents the period before the implementation of the Clean Air Action  
 699 (2010–2013); CAA Phase I and CAA Phase II represent the first (2014–2017) and second  
 700 (2018–2020) stages of the CAA, respectively. (b–d) Spatial distributions of the annual means  
 701 during the Pre-CAA, CAA Phase I, and CAA Phase II periods.

702

### 703 3.6 Uncertainties

704 Although the RegESM framework captures the overall spatiotemporal variations of  
 705 China’s terrestrial carbon sink in response to atmospheric composition changes, several uncer-  
 706 tainties remain that may influence the quantitative assessment of the individual and combined  
 707 effects of aerosols, O<sub>3</sub>, and nitrogen deposition.

708 First, this study only considered the direct radiative effects of aerosols, while aerosol–  
 709 cloud interactions were excluded. The first and second indirect effects of aerosols on cloud  
 710 formation and albedo involve large uncertainties (Haywood and Boucher, 2000) and were  
 711 therefore not represented in our simulations. However, observations have shown that terrestrial

712 carbon fluxes are highly sensitive to sky conditions and diffuse radiation changes (Oliphant et  
713 al., 2011; Yue and Unger, 2017). The omission of aerosol–cloud interactions may affect the  
714 magnitude and spatial pattern of aerosol impacts on radiation and photosynthesis, as cloud-  
715 mediated diffuse radiation responses remain uncertain. Future work should explicitly include  
716 aerosol–cloud–radiation feedbacks to better quantify their effects on ecosystem carbon ex-  
717 change.

718 Second, uncertainties remain in evaluating vegetation responses to O<sub>3</sub> exposure. Field-  
719 based O<sub>3</sub> fumigation experiments across China are still limited, making it difficult to compre-  
720 hensively assess ecosystem-level damage. In this study, the YIBs model applied different O<sub>3</sub>  
721 damage coefficients for plant functional types, and the parameterization has shown reasonable  
722 regional performance in simulating GPP–O<sub>3</sub> responses (Yue et al., 2017). Nevertheless, a wider  
723 range of site-level observations is required to constrain the O<sub>3</sub> damage functions across various  
724 vegetation types and climate zones at the national scale.

725 Third, nonlinear coupling among aerosols, O<sub>3</sub>, and nitrogen deposition introduces sys-  
726 temic uncertainty in estimating their combined effects. Aerosol reduction alters photolysis rates  
727 and thereby affects O<sub>3</sub> formation (Tang et al., 2017; Yan et al., 2023; Yang et al., 2022), while  
728 O<sub>3</sub> and nitrogen jointly regulate stomatal conductance, photosynthetic efficiency, and water-  
729 use dynamics (Sitch et al., 2007; Zhang et al., 2018). In addition, the coexisting effects of these  
730 three drivers may not be strictly additive. Aerosol effects and O<sub>3</sub> damage may be partly antag-  
731 onistic, as aerosol-induced changes in diffuse radiation, temperature, and vapor pressure deficit  
732 can modulate stomatal uptake and the physiological stress caused by O<sub>3</sub>. Nitrogen deposition  
733 may partly offset O<sub>3</sub>-induced reductions in plant productivity by alleviating nutrient limitation,  
734 whereas the interaction between aerosols and nitrogen deposition may vary regionally because  
735 nitrogen availability can influence the extent to which vegetation benefits from aerosol-induced  
736 radiation changes. These interactions may amplify or offset each other under changing climatic  
737 conditions, and the real-world coexisting effects of these atmospheric drivers may therefore  
738 differ from the linear sum of their independently quantified contributions. In the present study,  
739 the three factors were quantified separately to isolate their first-order effects, while a full as-  
740 essment of their two-way and three-way interactions would require a dedicated factorial

设置了格式: 下标

设置了格式: 下标

设置了格式: 下标

741 experimental framework. Therefore, although nonlinear interactions may modify the quantita-  
742 tive magnitudes of the simulated responses, the overall conclusion that the positive contribu-  
743 tions of aerosols and nitrogen deposition weakened while the suppressive influence of O<sub>3</sub> be-  
744 came increasingly important during 2010–2020 is expected to remain qualitatively robust.  
745 These limitations further emphasize the need for high-resolution, fully coupled chemistry–eco-  
746 system modeling frameworks to capture the co-evolution of multiple atmospheric processes.

设置了格式: 下标

747 In summary, despite these uncertainties, this study provides robust quantitative evidence  
748 that aerosols, O<sub>3</sub>, and nitrogen deposition jointly modified the magnitude and spatial distribu-  
749 tion of China’s terrestrial carbon sink during 2010–2020. Future efforts should focus on incor-  
750 porating aerosol–cloud interactions, expanding field-based O<sub>3</sub> response networks, and improv-  
751 ing representation of multi-process coupling and nonlinear interactions, to further constrain at-  
752 mospheric–biosphere feedbacks under China’s evolving air quality and carbon neutrality goals.

删除了: These interactions may amplify or offset each other under changing climatic conditions, emphasizing the need for high-resolution, fully coupled chemistry–ecosystem modeling frameworks to capture the co-evolution of multiple atmospheric processes.

删除了: and improving representation of multi-process coupling...

#### 754 4 Conclusions

755 This study employed the RegESM to quantify the effects of aerosol, surface O<sub>3</sub>, and ni-  
756 trogen deposition on China’s terrestrial carbon sink during 2010–2020. The model effectively  
757 reproduced the spatial and temporal variations of aerosol optical depth, O<sub>3</sub>, nitrogen deposition,  
758 and carbon fluxes, providing a solid basis for process-level attribution analysis.

759 Aerosols exerted a substantial positive influence on China’s terrestrial carbon sink. On  
760 average, aerosols enhanced GPP and NEP by 293.28 TgC yr<sup>-1</sup> (3.98%) and 17.93 TgC yr<sup>-1</sup>  
761 (4.49%), respectively, primarily through the diffuse radiation fertilization effect. The strongest  
762 enhancement appeared in southern and eastern China, where high aerosol loading and dense  
763 vegetation synergistically improved canopy light-use efficiency. Aerosol-induced surface cool-  
764 ing and reduced VPD further alleviated water stress and stimulated carbon uptake. The en-  
765 hancement peaked during 2015–2017, coinciding with elevated diffuse radiation fractions, and  
766 weakened slightly under cleaner atmospheric conditions after 2018.

767 In contrast, surface O<sub>3</sub> persistently suppressed ecosystem carbon uptake, reducing GPP  
768 and NEP by 749.44 TgC yr<sup>-1</sup> (10.17%) and 51.33 TgC yr<sup>-1</sup> (12.90%), respectively. The

776 strongest suppression occurred in southeastern and southwestern China, where dense forest  
777 ecosystems coincided with high O<sub>3</sub> concentrations. O<sub>3</sub>-induced damage peaked in 2018, con-  
778 sistent with the exceptionally high O<sub>3</sub> levels. Subsequent coordinated NO<sub>x</sub>-VOCs manage-  
779 ment under the second Clean Air Action partially mitigated O<sub>3</sub> levels and NEP suppression. O<sub>3</sub>  
780 exerted a strongly seasonal negative impact on NEP, with the strongest suppression occurring  
781 in summer.

782 Atmospheric nitrogen deposition enhanced the terrestrial carbon sink by 9.08% for GPP  
783 and 9.52% for NEP, with effects concentrated in southern and central China. The enhancement  
784 peaked around 2012, declined gradually after 2013 following reduced anthropogenic emissions,  
785 and leveled off after 2015, corresponding to a slower decline in deposition and a lagged eco-  
786 system response due to soil nitrogen accumulation. Seasonal variations showed stronger stim-  
787 ulation in summer and spring, while autumn and winter exhibited minor reductions linked to  
788 enhanced respiration.

789 During 2010–2020, the combined effects of aerosols, surface O<sub>3</sub>, and atmospheric nitro-  
790 gen deposition on China's terrestrial carbon sink exhibited marked interannual variability and  
791 a distinct transition under the Clean Air Action (CAA). The net atmospheric contribution de-  
792 clined from +8.22 Tg C yr<sup>-1</sup> during the Pre-CAA period (2010–2013) to +1.19 Tg C yr<sup>-1</sup> in  
793 Phase II (2018–2020), as the increasing suppression from O<sub>3</sub> (-53.15 Tg C yr<sup>-1</sup>) gradually offset  
794 the positive impacts of aerosols and nitrogen deposition. These results indicate that China's air-  
795 pollution control not only improved air quality but also altered atmospheric chemical compo-  
796 sition in ways that significantly affected ecosystem carbon uptake, with O<sub>3</sub> becoming the dom-  
797 inant limiting factor in the later period.

798 Overall, aerosols, O<sub>3</sub>, and nitrogen deposition exerted interconnected yet contrasting in-  
799 fluences on China's terrestrial carbon sink. Aerosols and nitrogen deposition enhanced carbon  
800 uptake through diffuse radiation and nutrient input, whereas O<sub>3</sub> caused physiological damage  
801 that suppressed it. The evolving interplay among these factors illustrates how emission reduc-  
802 tions, atmospheric chemistry, and ecosystem feedbacks jointly impact carbon sink dynamics  
803 under China's clean-air policies. These findings suggest that future air-quality management  
804 should move beyond single-pollutant control and place greater emphasis on coordinated multi-

805 pollutant strategies, particularly the synergistic reduction of NO<sub>x</sub> and VOCs, to limit O<sub>3</sub>-in-  
806 duced carbon sink suppression while sustaining gains in air quality. In addition, ecosystem  
807 carbon-sink responses should be incorporated into the evaluation of clean-air policies, espe-  
808 cially in ecologically sensitive regions of eastern and southern China, to better achieve co-  
809 benefits for air pollution mitigation and carbon neutrality goals.

设置了格式: 下标

删除了: Strengthening integrated O<sub>3</sub> control is therefore essential to secure co-benefits for air quality improvement and carbon neutrality goals

#### 810 **Data Availability Statement**

811 MODIS data are provided at <https://doi.org/10.5067/MODIS/MOD17A2H.006> (last access: 11  
812 May 2024; Running et al., 2015). AOD data come from the MODIS Level-3 monthly product  
813 (MOD08\_M3, Collection 6.1) available at [https://doi.org/10.5067/MODIS/MOD08\\_M3.061](https://doi.org/10.5067/MODIS/MOD08_M3.061)  
814 (last access: 5 November 2024; Platnick et al., 2015). WDCGG data are available at  
815 <https://doi.org/10.15138/wkgj-f215> (last access: 10 June 2024; Lan, 2023). ERA-Interim data  
816 are available at <https://doi.org/10.24381/cds.f2f5241d> (last access: 8 June 2024; Dee et al.,  
817 2011). The Carbon Tracker data can be accessed at <https://gml.noaa.gov/ccgg/carbontracker/>  
818 (last access: 21 June 2024; Jacobson et al., 2023). CNEMC data are provided at  
819 <https://www.cnemc.cn/en> (Kong et al., 2021).

#### 820 **Author contributions**

821 TW and NX designed the study. NX performed the analysis, conducted the evaluation, and  
822 drafted the manuscript. TW supervised the research and acquired funding. Both authors con-  
823 tributed to the interpretation of results and to reviewing and editing the manuscript.

#### 824 **Competing interests**

825 The corresponding author has stated that all the authors have no conflicts of interest.

#### 826 **Disclaimer**

827 Publisher's note: Copernicus Publications remains neutral with regard to jurisdictional claims  
828 made in the text, published maps, institutional affiliations, or any other geographical represen-  
829 tation in this paper. The authors bear the ultimate responsibility for providing appropriate place  
830 names. Views expressed in the text are those of the authors and do not necessarily reflect the

834 views of the publisher.

### 835 **Acknowledgments**

836 We would like to acknowledge the anthropogenic emission inventory support from Tsinghua  
837 University and the observed data from the China National Environmental Monitoring Center.  
838 We also gratefully acknowledge a wide range of other institutional partners.

### 839 **Financial support**

840 This work was supported by the National Key Basic Research Development Program of China  
841 (2024YFC3711905) and the National Natural Science Foundation of China (42477103).

### 842 **References**

- 843 Cao, S., He, Y., Zhang, L., Sun, Q., Zhang, Y., Li, H., Wei, X., and Liu, Y.: Spatiotemporal  
844 dynamics of vegetation net ecosystem productivity and its response to drought in  
845 Northwest China, *GIScience & Remote Sensing*, 60, 2194597,  
846 <https://doi.org/10.1080/15481603.2023.2194597>, 2023.
- 847 Cen, X., He, N., Van Sundert, K., Yu, K., Li, M., Xu, L., He, L., and Butterbach-Bahl, K.:  
848 Global patterns of nitrogen saturation in forests, *One Earth*, 8,  
849 <https://doi.org/10.1016/j.oneear.2024.10.007>, 2025.
- 850 Chen, H., Li, D., Gurmessa, G. A., Yu, G., Li, L., Zhang, W., Fang, H., and Mo, J.: Effects of  
851 nitrogen deposition on carbon cycle in terrestrial ecosystems of China: A meta-analysis,  
852 *Environ. Pollut.*, 206, 352-360, <https://doi.org/10.1016/j.envpol.2015.07.033>, 2015.
- 853 Dee, D. P., Uppala, S. M., Simmons, A. J., Berrisford, P., Poli, P., Kobayashi, S., Andrae, U.,  
854 Balmaseda, M. A., Balsamo, G., Bauer, P., Bechtold, P., Beljaars, A. C. M., van de Berg,  
855 L., Bidlot, J., Bormann, N., Delsol, C., Dragani, R., Fuentes, M., Geer, A. J., Haimberger,  
856 L., Healy, S. B., Hersbach, H., Hólm, E. V., Isaksen, L., Kållberg, P., Köhler, M.,  
857 Matricardi, M., McNally, A. P., Monge-Sanz, B. M., Morcrette, J. J., Park, B. K., Peubey,  
858 C., de Rosnay, P., Tavolato, C., Thépaut, J. N., and Vitart, F.: The ERA-Interim reanalysis:  
859 configuration and performance of the data assimilation system, *QJRM*, 137, 553-597,  
860 <https://doi.org/10.1002/qj.828>, 2011.

861 Doughty, C. E., Flanner, M. G., and Goulden, M. L.: Effect of smoke on subcanopy shaded  
862 light, canopy temperature, and carbon dioxide uptake in an Amazon rainforest, *Global*  
863 *Biogeochemical Cycles*, 24, <https://doi.org/10.1029/2009gb003670>, 2010.

864 Emmons, L. K., Walters, S., Hess, P. G., Lamarque, J. F., Pfister, G. G., Fillmore, D., Granier,  
865 C., Guenther, A., Kinnison, D., Laepple, T., Orlando, J., Tie, X., Tyndall, G., Wiedinmyer,  
866 C., Baughcum, S. L., and Kloster, S.: Description and evaluation of the Model for Ozone  
867 and Related chemical Tracers, version 4 (MOZART-4), *Geosci. Model Dev.*, 3, 43-67,  
868 <https://doi.org/10.5194/gmd-3-43-2010>, 2010.

869 Feng, Z., Hu, E., Wang, X., Jiang, L., and Liu, X.: Ground-level O<sub>3</sub> pollution and its impacts  
870 on food crops in China: A review, *Environ. Pollut.*, 199, 42-48,  
871 <https://doi.org/10.1016/j.envpol.2015.01.016>, 2015.

872 Friedlingstein, P., O'Sullivan, M., Jones, M. W., Andrew, R. M., Bakker, D. C. E., Hauck, J.,  
873 Landschützer, P., Le Quéré, C., Lujckx, I. T., Peters, G. P., Peters, W., Pongratz, J.,  
874 Schwingshackl, C., Sitch, S., Canadell, J. G., Ciais, P., Jackson, R. B., Alin, S. R., Anthoni,  
875 P., Barbero, L., Bates, N. R., Becker, M., Bellouin, N., Decharme, B., Bopp, L., Brasika,  
876 I. B. M., Cadule, P., Chamberlain, M. A., Chandra, N., Chau, T.-T.-T., Chevallier, F., Chini,  
877 L. P., Cronin, M., Dou, X., Enyo, K., Evans, W., Falk, S., Feely, R. A., Feng, L., Ford, D.  
878 J., Gasser, T., Ghattas, J., Gkritzalis, T., Grassi, G., Gregor, L., Gruber, N., Gürses, Ö.,  
879 Harris, I., Hefner, M., Heinke, J., Houghton, R. A., Hurtt, G. C., Iida, Y., Ilyina, T.,  
880 Jacobson, A. R., Jain, A., Jarníková, T., Jersild, A., Jiang, F., Jin, Z., Joos, F., Kato, E.,  
881 Keeling, R. F., Kennedy, D., Klein Goldewijk, K., Knauer, J., Korsbakken, J. I., Körtzinger,  
882 A., Lan, X., Lefèvre, N., Li, H., Liu, J., Liu, Z., Ma, L., Marland, G., Mayot, N., McGuire,  
883 P. C., McKinley, G. A., Meyer, G., Morgan, E. J., Munro, D. R., Nakaoka, S.-I., Niwa, Y.,  
884 O'Brien, K. M., Olsen, A., Omar, A. M., Ono, T., Paulsen, M., Pierrot, D., Pöcöck, K.,  
885 Poulter, B., Powis, C. M., Rehder, G., Resplandy, L., Robertson, E., Rödenbeck, C., Rosan,  
886 T. M., Schwinger, J., Séférian, R., Smallman, T. L., Smith, S. M., Sospedra-Alfonso, R.,  
887 Sun, Q., Sutton, A. J., Sweeney, C., Takao, S., Tans, P. P., Tian, H., Tilbrook, B., Tsujino,  
888 H., Tubiello, F., van der Werf, G. R., van Ooijen, E., Wanninkhof, R., Watanabe, M.,  
889 Wimart-Rousseau, C., Yang, D., Yang, X., Yuan, W., Yue, X., Zächle, S., Zeng, J., and

890 Zheng, B.: Global Carbon Budget 2023, *Earth System Science Data*, 15, 5301-5369,  
891 <https://doi.org/10.5194/essd-15-5301-2023>, 2023.

892 Geng, G. N., Liu, Y. X., Liu, Y., Liu, S. G., Cheng, J., Yan, L., Wu, N. N., Hu, H. W., Tong, D.,  
893 Zheng, B., Yin, Z. C., He, K. B., and Zhang, Q.: Efficacy of China's clean air actions to  
894 tackle PM<sub>2.5</sub> pollution between 2013 and 2020, *Nature Geoscience*, 17,  
895 <https://doi.org/10.1038/s41561-024-01540-z>, 2024.

896 Giorgi, F., Coppola, E., Solmon, F., Mariotti, L., Sylla, M. B., Bi, X., Elguindi, N., Diro, G. T.,  
897 Nair, V., Giuliani, G., Turuncoglu, U. U., Cozzini, S., Guttler, I., O'Brien, T. A., Tawfik,  
898 A. B., Shalaby, A., Zakey, A. S., Steiner, A. L., Stordal, F., Sloan, L. C., and Brankovic,  
899 C.: RegCM4: model description and preliminary tests over multiple CORDEX domains,  
900 *Clim. Res.*, 52, 7-29, <https://doi.org/10.3354/cr01018>, 2012.

901 Gu, L. H., Baldocchi, D. D., Wofsy, S. C., Munger, J. W., Michalsky, J. J., Urbanski, S. P., and  
902 Boden, T. A.: Response of a deciduous forest to the Mount Pinatubo eruption: Enhanced  
903 photosynthesis, *Science*, 299, 2035-2038, <https://doi.org/10.1126/science.1078366>, 2003.

904 Hao, Y., Meng, X., Yu, X., Lei, M., Li, W., Yang, W., Shi, F., and Xie, S.: Quantification of  
905 primary and secondary sources to PM<sub>2.5</sub> using an improved source regional apportionment  
906 method in an industrial city, China, *Sci. Total Environ.*, 706,  
907 <https://doi.org/10.1016/j.scitotenv.2019.135715>, 2020.

908 Haywood, J. and Boucher, O.: Estimates of the direct and indirect radiative forcing due to  
909 tropospheric aerosols: A review, *Reviews of Geophysics*, 38, 513-543,  
910 <https://doi.org/10.1029/1999rg000078>, 2000.

911 He, M. Z., Kimball, J. S., Maneta, M. P., Maxwell, B. D., Moreno, A., Begueria, S., and Wu,  
912 X. C.: Regional Crop Gross Primary Productivity and Yield Estimation Using Fused  
913 Landsat-MODIS Data, *Remote Sens.*, 10, 372, <https://doi.org/10.3390/rs10030372>, 2018.

914 Hersbach, H., Bell, B., Berrisford, P., Hirahara, S., Horányi, A., Muñoz-Sabater, J., Nicolas, J.,  
915 Peubey, C., Radu, R., Schepers, D., Simmons, A., Soci, C., Abdalla, S., Abellan, X.,  
916 Balsamo, G., Bechtold, P., Biavati, G., Bidlot, J., Bonavita, M., De Chiara, G., Dahlgren,  
917 P., Dee, D., Diamantakis, M., Dragani, R., Flemming, J., Forbes, R., Fuentes, M., Geer,  
918 A., Haimberger, L., Healy, S., Hogan, R. J., Hólm, E., Janisková, M., Keeley, S., Laloyaux,

919 P., Lopez, P., Lupu, C., Radnoti, G., de Rosnay, P., Rozum, I., Vamborg, F., Villaume, S.,  
920 and Thépaut, J. N.: The ERA5 global reanalysis, *QJRMS*, 146, 1999-2049,  
921 <https://doi.org/10.1002/qj.3803>, 2020.

922 Horowitz, L. W., Walters, S., Mauzerall, D. L., Emmons, L. K., Rasch, P. J., Granier, C., Tie,  
923 X. X., Lamarque, J. F., Schultz, M. G., Tyndall, G. S., Orlando, J. J., and Brasseur, G. P.:  
924 A global simulation of tropospheric ozone and related tracers: Description and evaluation  
925 of MOZART, version 2, *J. Geophys. Res.: Atmos.*, 108, 4784,  
926 <https://doi.org/10.1029/2002jd002853>, 2003.

927 Jacobson, A. R., Schuldt, K. N., Tans, P., Arlyn Andrews, Miller, J. B., Oda, T., Mund, J., Weir,  
928 B., Ott, L., Aalto, T., Abshire, J. B., Aikin, K., Aoki, S., Apadula, F., Arnold, S., Baier, B.,  
929 Bartyzel, J., Beyersdorf, A., Biermann, T., ... Miroslaw Zimnoch.: CarbonTracker  
930 CT2022, NOAA Global Monitoring Laboratory, [data set],  
931 <https://doi.org/10.25925/Z1GJ-3254>, 2023.

932 Jung, M., Reichstein, M., Schwalm, C. R., Huntingford, C., Sitch, S., Ahlstrom, A., Arneeth, A.,  
933 Camps-Valls, G., Ciais, P., Friedlingstein, P., Gans, F., Ichii, K., Ain, A. K. J., Kato, E.,  
934 Papale, D., Poulter, B., Raduly, B., Rodenbeck, C., Tramontana, G., Viovy, N., Wang, Y.-  
935 P., Weber, U., Zaehle, S., and Zeng, N.: Compensatory water effects link yearly global  
936 land CO<sub>2</sub> sink changes to temperature, *Nature*, 541, 516-520,  
937 <https://doi.org/10.1038/nature20780>, 2017.

938 Kong, L., Tang, X., Zhu, J., Wang, Z. F., Li, J. J., Wu, H. J., Wu, Q. Z., Chen, H. S., Zhu, L. L.,  
939 Wang, W., Liu, B., Wang, Q., Chen, D. H., Pan, Y. P., Song, T., Li, F., Zheng, H. T., Jia,  
940 G. L., Lu, M. M., Wu, L., and Carmichael, G. R.: A 6-year-long (2013-2018) high-  
941 resolution air quality reanalysis dataset in China based on the assimilation of surface  
942 observations from CNEMC, *Earth System Science Data*, 13, 529-570,  
943 <https://doi.org/10.5194/essd-13-529-2021>, 2021.

944 Kuniyal, J. C. and Guleria, R. P.: The current state of aerosol-radiation interactions: A mini  
945 review, *Journal of Aerosol Science*, 130, 45-54,  
946 <https://doi.org/10.1016/j.jaerosci.2018.12.010>, 2019.

947 Lan, X.: Atmospheric Carbon Dioxide Dry Air Mole Fractions from the NOAA GML Carbon

948 Cycle Cooperative Global Air Sampling Network, 1968-2022, Version: 2023-08-28, [data  
949 set], <https://doi.org/10.15138/wkgj-f215>, 2023.

950 Lawrence, P. J. and Chase, T. N.: Representing a new MODIS consistent land surface in the  
951 Community Land Model (CLM 3.0), *J. Geophys. Res.: Biogeosci.*, 112, G01023,  
952 <https://doi.org/10.1029/2006jg000168>, 2007.

953 Lei, Y., Yue, X., Wang, Z., Liao, H., Zhang, L., Tian, C., Zhou, H., Zhong, J., Guo, L., Che, H.,  
954 and Zhang, X.: Mitigating ozone damage to ecosystem productivity through sectoral and  
955 regional emission controls: a case study in the Yangtze River Delta, China, *Environmental*  
956 *Research Letters*, 17, <https://doi.org/10.1088/1748-9326/ac6ff7>, 2022.

957 Levy, R. C., Mattoo, S., Munchak, L. A., Remer, L. A., Sayer, A. M., Patadia, F., and Hsu, N.  
958 C.: The Collection 6 MODIS aerosol products over land and ocean, *Atmospheric*  
959 *Measurement Techniques*, 6, 2989-3034, <https://doi.org/10.5194/amt-6-2989-2013>, 2013.

960 Li, M., Huang, X., Yan, D., Lai, S., Zhang, Z., Zhu, L., Lu, Y., Jiang, X., Wang, N., Wang, T.,  
961 Song, Y., and Ding, A.: Coping with the concurrent heatwaves and ozone extremes in  
962 China under a warming climate, *Science Bulletin*, 69, 2938-2947,  
963 <https://doi.org/10.1016/j.scib.2024.05.034>, 2024.

964 Li, M., Liu, H., Geng, G. N., Hong, C. P., Liu, F., Song, Y., Tong, D., Zheng, B., Cui, H. Y.,  
965 Man, H. Y., Zhang, Q., and He, K. B.: Anthropogenic emission inventories in China: a  
966 review, *National Science Review*, 4, 834-866, <https://doi.org/10.1093/nsr/nwx150>, 2017.

967 Li, X., Liang, H., and Cheng, W.: Spatio-Temporal Variation in AOD and Correlation Analysis  
968 with PAR and NPP in China from 2001 to 2017, *Remote Sens.*, 12,  
969 <https://doi.org/10.3390/rs12060976>, 2020.

970 Liu, H., Liu, S., Xue, B., Lv, Z., Meng, Z., Yang, X., Xue, T., Yu, Q., and He, K.: Ground-level  
971 ozone pollution and its health impacts in China, *Atmos. Environ.*, 173, 223-230,  
972 <https://doi.org/10.1016/j.atmosenv.2017.11.014>, 2018.

973 Liu, L., Wen, Z., Liu, S., Zhang, X., and Liu, X.: Decline in atmospheric nitrogen deposition  
974 in China between 2010 and 2020, *Nature Geoscience*, 17, <https://doi.org/10.1038/s41561-024-01484-4>, 2024.

975  
976 Liu, M., Shang, F., Lu, X., Huang, X., Song, Y., Liu, B., Zhang, Q., Liu, X., Cao, J., Xu, T.,

977 Wang, T., Xu, Z., Xu, W., Liao, W., Kang, L., Cai, X., Zhang, H., Dai, Y., and Zhu, T.:  
978 Unexpected response of nitrogen deposition to nitrogen oxide controls and implications  
979 for land carbon sink, *Nature Communications*, 13, [https://doi.org/10.1038/s41467-022-](https://doi.org/10.1038/s41467-022-30854-y)  
980 30854-y, 2022.

981 Liu, X., Zhang, Y., Han, W., Tang, A., Shen, J., Cui, Z., Vitousek, P., Erisman, J. W., Goulding,  
982 K., Christie, P., Fangmeier, A., and Zhang, F.: Enhanced nitrogen deposition over China,  
983 *Nature*, 494, 459-462, <https://doi.org/10.1038/nature11917>, 2013.

984 Lu, X., Hou, E., Guo, J., Gilliam, F. S., Li, J., Tang, S., and Kuang, Y.: Nitrogen addition  
985 stimulates soil aggregation and enhances carbon storage in terrestrial ecosystems of China:  
986 A meta-analysis, *Global Change Biology*, 27, 2780-2792,  
987 <https://doi.org/10.1111/gcb.15604>, 2021.

988 Lu, X., Jiang, H., Liu, J., Zhang, X., Jin, J., Zhu, Q., Zhang, Z., and Peng, C.: Simulated effects  
989 of nitrogen saturation on the global carbon budget using the IBIS model, *Sci. Rep.*, 6,  
990 <https://doi.org/10.1038/srep39173>, 2016.

991 Lu, X., Zhang, L., Wang, X. L., Gao, M., Li, K., Zhang, Y. Z., Yue, X., and Zhang, Y. H.: Rapid  
992 Increases in Warm-Season Surface Ozone and Resulting Health Impact in China Since  
993 2013, *Environmental Science & Technology Letters*, 7, 240-247,  
994 <https://doi.org/10.1021/acs.estlett.0c00171>, 2020.

995 Luo, Y. X., Zheng, X. B., Zhao, T. L., and Chen, J.: A climatology of aerosol optical depth over  
996 China from recent 10 years of MODIS remote sensing data, *IJCLI*, 34, 863-870,  
997 <https://doi.org/10.1002/joc.3728>, 2014.

998 Ma, D. Y., Wang, T. J., Wu, H., Qu, Y. W., Liu, J., Liu, J. E., Li, S., Zhuang, B. L., Li, M. M.,  
999 and Xie, M.: The effect of anthropogenic emission, meteorological factors, and  
1000 carbondioxide on the surface ozone increase in China from 2008 to 2018 during theEast  
1001 Asia summer monsoon season, *Atmos. Chem. Phys.*, 23, 6525-6544,  
1002 <https://doi.org/10.5194/acp-23-6525-2023>, 2023.

1003 Madani, N., Kimball, J. S., Affleck, D. L. R., Kattge, J., Graham, J., van Bodegom, P. M., Reich,  
1004 P. B., and Running, S. W.: Improving ecosystem productivity modeling through spatially  
1005 explicit estimation of optimal light use efficiency, *J. Geophys. Res.: Biogeosci.*, 119,

1006 1755-1769, <https://doi.org/10.1002/2014jg002709>, 2014.

1007 Mercado, L. M., Bellouin, N., Sitch, S., Boucher, O., Huntingford, C., Wild, M., and Cox, P.  
1008 M.: Impact of changes in diffuse radiation on the global land carbon sink, *Nature*, 458,  
1009 1014-U1087, <https://doi.org/10.1038/nature07949>, 2009.

1010 Oliphant, A. J., Dragoni, D., Deng, B., Grimmond, C. S. B., Schmid, H. P., and Scott, S. L.:  
1011 The role of sky conditions on gross primary production in a mixed deciduous forest, *Agric.*  
1012 *For. Meteorol.*, 151, 781-791, <https://doi.org/10.1016/j.agrformet.2011.01.005>, 2011.

1013 Peng, X., Wei, W., Niu, S., Huang, Y., and Chen, L.: Divergent impact of long-term  
1014 anthropogenic nitrogen inputs on global particulate and mineral-associated organic carbon,  
1015 *Ecological Processes*, 14, <https://doi.org/10.1186/s13717-025-00624-x>, 2025.

1016 Peters, W., Jacobson, A. R., Sweeney, C., Andrews, A. E., Conway, T. J., Masarie, K., Miller,  
1017 J. B., Bruhwiler, L. M. P., Petron, G., Hirsch, A. I., Worthy, D. E. J., van der Werf, G. R.,  
1018 Randerson, J. T., Wennberg, P. O., Krol, M. C., and Tans, P. P.: An atmospheric perspective  
1019 on North American carbon dioxide exchange: CarbonTracker, *Proc. Natl. Acad. Sci.*  
1020 *U.S.A.*, 104, 18925-18930, <https://doi.org/10.1073/pnas.0708986104>, 2007.

1021 Piao, S., He, Y., Wang, X., and Chen, F.: Estimation of China's terrestrial ecosystem carbon  
1022 sink: Methods, progress and prospects, *Science China Earth Sciences*, 65, 641-651,  
1023 <https://doi.org/10.1007/s11430-021-9892-6>, 2022.

1024 Piao, S., Sitch, S., Ciais, P., Friedlingstein, P., Peylin, P., Wang, X., Ahlstrom, A., Anav, A.,  
1025 Canadell, J. G., Cong, N., Huntingford, C., Jung, M., Levis, S., Levy, P. E., Li, J., Lin, X.,  
1026 Lomas, M. R., Lu, M., Luo, Y., Ma, Y., Myneni, R. B., Poulter, B., Sun, Z., Wang, T.,  
1027 Viovy, N., Zaehle, S., and Zeng, N.: Evaluation of terrestrial carbon cycle models for their  
1028 response to climate variability and to CO<sub>2</sub> trends, *Glob. Chang. Biol.*, 19, 2117-2132,  
1029 <https://doi.org/10.1111/gcb.12187>, 2013.

1030 Platnick, S., King, M., and Hubanks, P.: MOD08\_M3 - MODIS/Terra Aerosol Cloud Water  
1031 Vapor Ozone Monthly L3 Global 1Deg CMG, NASA MODIS Adaptive Processing  
1032 System, Goddard Space Flight Center [data set], USA,  
1033 [https://doi.org/10.5067/MODIS/MOD08\\_M3.061](https://doi.org/10.5067/MODIS/MOD08_M3.061), 2015.

1034 Post, E., Steinman, B. A., and Mann, M. E.: Acceleration of phenological advance and warming

1035 with latitude over the past century, *Sci. Rep.*, 8, 3927, <https://doi.org/10.1038/s41598-018->  
1036 22258-0, 2018.

1037 Ren, W., Tian, H. Q., Tao, B., Huang, Y., and Pan, S. F.: China's crop productivity and soil  
1038 carbon storage as influenced by multifactor global change, *Global Change Biology*, 18,  
1039 2945-2957, <https://doi.org/10.1111/j.1365-2486.2012.02741.x>, 2012.

1040 Ren, W., Banger, K., Tao, B., Yang, J., Huang, Y., and Tian, H.: Global pattern and change of  
1041 cropland soil organic carbon during 1901-2010: Roles of climate, atmospheric chemistry,  
1042 land use and management, *Geography and Sustainability*, 1, 59-69,  
1043 <https://doi.org/10.1016/j.geosus.2020.03.001>, 2020.

1044 Running, S., Mu, Q., Zhao, M.: MOD17A2H MODIS/Terra Gross Primary Productivity 8-Day  
1045 L4 Global 500m SIN Grid V006, NASA EOSDIS Land Processes Distributed Active  
1046 Archive Center, [data set], <https://doi.org/10.5067/MODIS/MOD17A2H.006>, 2015.

1047 Shalaby, A., Zakey, A. S., Tawfik, A. B., Solmon, F., Giorgi, F., Stordal, F., Sillman, S., Zaveri,  
1048 R. A., and Steiner, A. L.: Implementation and evaluation of online gas-phase chemistry  
1049 within a regional climate model (RegCM-CHEM4), *Geosci. Model Dev.*, 5, 741-760,  
1050 <https://doi.org/10.5194/gmd-5-741-2012>, 2012.

1051 Shang, F., Liu, M. X., Song, Y., Lu, X. J., Zhang, Q., Matsui, H., Liu, L. L., Ding, A. J., Huang,  
1052 X., Liu, X. J., Cao, J. J., Wang, Z. F., Dai, Y. J., Kang, L., Cai, X. H., Zhang, H. S., and  
1053 Zhu, T.: Substantial nitrogen abatement accompanying decarbonization suppresses  
1054 terrestrial carbon sinks in China, *Nature Communications*, 15,  
1055 <https://doi.org/10.1038/s41467-024-52152-5>, 2024.

1056 Shu, Y., Liu, S., Wang, Z., Xiao, J., Shi, Y., Peng, X., Gao, H., Wang, Y., Yuan, W., Yan, W.,  
1057 Ning, Y., and Li, Q.: Effects of Aerosols on Gross Primary Production from Ecosystems  
1058 to the Globe, *Remote Sens.*, 14, <https://doi.org/10.3390/rs14122759>, 2022.

1059 Sitch, S., Cox, P. M., Collins, W. J., and Huntingford, C.: Indirect radiative forcing of climate  
1060 change through ozone effects on the land-carbon sink, *Nature*, 448, 791-U794,  
1061 <https://doi.org/10.1038/nature06059>, 2007.

1062 Strada, S. and Unger, N.: Potential sensitivity of photosynthesis and isoprene emission to direct  
1063 radiative effects of atmospheric aerosol pollution, *Atmos. Chem. Phys.*, 16, 4213-4234,

1064 <https://doi.org/10.5194/acp-16-4213-2016>, 2016.

1065 Tang, M. J., Huang, X., Lu, K. D., Ge, M. F., Li, Y. J., Cheng, P., Zhu, T., Ding, A. J., Zhang,  
1066 Y. H., Gligorovski, S., Song, W., Ding, X., Bi, X. H., and Wang, X. M.: Heterogeneous  
1067 reactions of mineral dust aerosol: implications for tropospheric oxidation capacity, *Atmos.*  
1068 *Chem. Phys.*, 17, 11727-11777, <https://doi.org/10.5194/acp-17-11727-2017>, 2017.

1069 Tu, M., Liu, Z., He, C., Fang, Z., and Lu, W.: The relationships between urban landscape  
1070 patterns and fine particulate pollution in China: A multiscale investigation using a  
1071 geographically weighted regression model, *Journal of Cleaner Production*, 237,  
1072 <https://doi.org/10.1016/j.jclepro.2019.117744>, 2019.

1073 Unger, N., Yue, X., and Harper, K. L.: Aerosol climate change effects on land ecosystem  
1074 services, *Faraday Discuss.*, 200, 121-142, <https://doi.org/10.1039/c7fd00033b>, 2017.

1075 Unger, N., Zheng, Y., Yue, X., and Harper, K. L.: Mitigation of ozone damage to the world's  
1076 land ecosystems by source sector, *Nature Climate Change*, 10, 134+,  
1077 <https://doi.org/10.1038/s41558-019-0678-3>, 2020.

1078 Wang, J., Dong, J., Yi, Y., Lu, G., Oyler, J., Smith, W. K., Zhao, M., Liu, J., and Running, S.:  
1079 Decreasing net primary production due to drought and slight decreases in solar radiation  
1080 in China from 2000 to 2012, *J. Geophys. Res.: Biogeosci.*, 122, 261-278,  
1081 <https://doi.org/10.1002/2016jg003417>, 2017.

1082 Wang, K., Zhang, Y., Yahya, K., Wu, S. Y., and Grell, G.: Implementation and initial application  
1083 of new chemistry-aerosol options in WRF/Chem for simulating secondary organic  
1084 aerosols and aerosol indirect effects for regional air quality, *Atmos. Environ.*, 115, 716-  
1085 732, <https://doi.org/10.1016/j.atmosenv.2014.12.007>, 2015.

1086 Wang, X., Wu, J., Chen, M., Xu, X., Wang, Z., Wang, B., Wang, C., Piao, S., Lin, W., Miao,  
1087 G., Deng, M., Qiao, C., Wang, J., Xu, S., and Liu, L.: Field evidences for the positive  
1088 effects of aerosols on tree growth, *Global Change Biology*, 24, 4983-4992,  
1089 <https://doi.org/10.1111/gcb.14339>, 2018.

1090 Wang, Y., Ni, J., Xu, K., Zhang, H., Gong, X., and He, C.: Intricate synergistic effects between  
1091 air pollution and carbon emission: An emerging evidence from China, *Environ. Pollut.*,  
1092 349, <https://doi.org/10.1016/j.envpol.2024.123851>, 2024.

1093 Wittig, V. E., Ainsworth, E. A., and Long, S. P.: To what extent do current and projected  
1094 increases in surface ozone affect photosynthesis and stomatal conductance of trees? A  
1095 meta-analytic review of the last 3 decades of experiments, *Plant Cell and Environment*,  
1096 30, 1150-1162, <https://doi.org/10.1111/j.1365-3040.2007.01717.x>, 2007.

1097 Xia, J., Xia, X., Wang, X., Ju, W., Lin, Z., Qin, Z., Sang, Y., Yan, Y., Yuan, W., Yue, X., Zhang,  
1098 H., Zhou, H., and Zhu, Q.: China Land Carbon Budget (CLCB1.0): a comprehensive  
1099 estimate of the land carbon budget in China, *National Science Review*, 12,  
1100 <https://doi.org/10.1093/nsr/nwaf052>, 2025.

1101 Xie, N., Wang, T., Xie, X., Yue, X., Giorgi, F., Zhang, Q., Ma, D., Song, R., Xu, B., Li, S.,  
1102 Zhuang, B., Li, M., Xie, M., Kilifarska, N. A., Gadzhev, G., and Dimitrova, R.: The  
1103 regional climate-chemistry-ecology coupling model RegCM-Chem (v4.6)-YIBs (v1.0):  
1104 development and application, *Geosci. Model Dev.*, 17, 3259-3277,  
1105 <https://doi.org/10.5194/gmd-17-3259-2024>, 2024.

1106 Xie, N. H., Wang, T. J., Xie, M., Ma, D. Y., Zhang, Q., Li, M. M., Li, S., Zhuang, B. L., Kalsoom,  
1107 U., Kilifarska, N. A., Gadzhev, G., Dimitrova, R., Melas, D., and Karatzas, K.: Carbon  
1108 Sink of Terrestrial Ecosystems in China During 2010-2020: Spatiotemporal Variability  
1109 and Climate Impact, *J. Geophys. Res.: Atmos.*, 130,  
1110 <https://doi.org/10.1029/2025jd043405>, 2025.

1111 Xie, X., Wang, T., Yue, X., Li, S., Zhuang, B., and Wang, M.: Effects of atmospheric aerosols  
1112 on terrestrial carbon fluxes and CO<sub>2</sub> concentrations in China, *Atmos. Res.*,  
1113 237, <https://doi.org/10.1016/j.atmosres.2020.104859>, 2020.

1114 Xie, X. D., Wang, T. J., Yue, X., Li, S., Zhuang, B. L., Wang, M. H., and Yang, X. Q.: Numerical  
1115 modeling of ozone damage to plants and its effects on atmospheric CO<sub>2</sub> in China, *Atmos.*  
1116 *Environ.*, 217, 116970, <https://doi.org/10.1016/j.atmosenv.2019.116970>, 2019.

1117 Xue, T., Liu, J., Zhang, Q., Geng, G., Zheng, Y., Tong, D., Liu, Z., Guan, D., Bo, Y., Zhu, T.,  
1118 He, K., and Hao, J.: Rapid improvement of PM<sub>2.5</sub> pollution and associated  
1119 health benefits in China during 2013-2017, *Science China-Earth Sciences*, 62, 1847-1856,  
1120 <https://doi.org/10.1007/s11430-018-9348-2>, 2019.

1121 Yan, S. Q., Zhu, B., Shi, S. S., Lu, W., Gao, J. H., Kang, H. Q., and Liu, D. Y.: Impact of aerosol

1122 optics on vertical distribution of ozone in autumn over Yangtze River Delta, *Atmos. Chem.*  
1123 *Phys.*, 23, 5177-5190, <https://doi.org/10.5194/acp-23-5177-2023>, 2023.

1124 Yang, H., Chen, L., Liao, H., Zhu, J., Wang, W. J., and Li, X.: Impacts of aerosol-photolysis  
1125 interaction and aerosol-radiation feedback on surface-layer ozone in North China during  
1126 multi-pollutant air pollution episodes, *Atmos. Chem. Phys.*, 22, 4101-4116,  
1127 <https://doi.org/10.5194/acp-22-4101-2022>, 2022.

1128 Yu, G., Jia, Y., He, N., Zhu, J., Chen, Z., Wang, Q., Piao, S., Liu, X., He, H., Guo, X., Wen, Z.,  
1129 Li, P., Ding, G., and Goulding, K.: Stabilization of atmospheric nitrogen deposition in  
1130 China over the past decade, *Nature Geoscience*, 12, 424-+,  
1131 <https://doi.org/10.1038/s41561-019-0352-4>, 2019.

1132 Yuan, X., Chen, X., Ochege, F. U., Hamdi, R., Tabari, H., Li, B., He, B., Zhang, C., De Maeyer,  
1133 P., and Luo, G.: Weakening of global terrestrial carbon sequestration capacity under  
1134 increasing intensity of warm extremes, *Nature Ecology & Evolution*, 9,  
1135 <https://doi.org/10.1038/s41559-024-02576-5>, 2025.

1136 Yue, H., He, C., Huang, Q., Yin, D., and Bryan, B. A.: Stronger policy required to substantially  
1137 reduce deaths from PM<sub>2.5</sub> pollution in China, *Nature Communications*, 11,  
1138 <https://doi.org/10.1038/s41467-020-15319-4>, 2020.

1139 Yue, K., Peng, Y., Peng, C., Yang, W., Peng, X., and Wu, F.: Stimulation of terrestrial ecosystem  
1140 carbon storage by nitrogen addition: a meta-analysis, *Sci. Rep.*, 6,  
1141 <https://doi.org/10.1038/srep19895>, 2016.

1142 Yue, X. and Unger, N.: The Yale Interactive terrestrial Biosphere model version 1.0: description,  
1143 evaluation and implementation into NASA GISS ModelE2, *Geosci. Model Dev.*, 8, 2399-  
1144 2417, <https://doi.org/10.5194/gmd-8-2399-2015>, 2015.

1145 Yue, X. and Unger, N.: Aerosol optical depth thresholds as a tool to assess diffuse radiation  
1146 fertilization of the land carbon uptake in China, *Atmos. Chem. Phys.*, 17, 1329-1342,  
1147 <https://doi.org/10.5194/acp-17-1329-2017>, 2017.

1148 Yue, X., Zhang, T., and Shao, C.: Afforestation increases ecosystem productivity and carbon  
1149 storage in China during the 2000s, *Agric. For. Meteorol.*, 296, 108227,  
1150 <https://doi.org/10.1016/j.agrformet.2020.108227>, 2021.

1151 Yue, X., Unger, N., Harper, K., Xia, X., Liao, H., Zhu, T., Xiao, J., Feng, Z., and Li, J.: Ozone  
1152 and haze pollution weakens net primary productivity in China, *Atmos. Chem. Phys.*, 17,  
1153 6073-6089, <https://doi.org/10.5194/acp-17-6073-2017>, 2017.

1154 Zhang, F. M., Chen, J. M., Chen, J. Q., Gough, C. M., Martin, T. A., and Dragoni, D.:  
1155 Evaluating spatial and temporal patterns of MODIS GPP over the conterminous US  
1156 against flux measurements and a process model, *Remote Sensing of Environment*, 124,  
1157 717-729, <https://doi.org/10.1016/j.rse.2012.06.023>, 2012.

1158 Zhang, Q., Wang, T. J., Wu, H., Qu, Y. W., Xie, M., Li, S., Zhuang, B. L., Li, M. M., and  
1159 Kilifarska, N. A.: Radiative and Chemical Effects of Non-Homogeneous Methane on  
1160 Terrestrial Carbon Fluxes in Asia, *J. Geophys. Res.: Atmos.*, 129,  
1161 <https://doi.org/10.1029/2023jd040204>, 2024.

1162 Zhang, Q., Wang, T., Zhang, Z., Xu, X., Xie, N., Zhuang, B., Li, S., Gao, L., Li, M., and Xie,  
1163 M.: Methane Emissions in Asian Wetlands During 2010–2020: Insights From an Online-  
1164 Coupled Microbial Functional-Group-Based Model, *Earth's Future*, 13,  
1165 <https://doi.org/10.1029/2025ef005991>, 2025.

1166 Zhang, W. W., Wang, M., Wang, A. Y., Yin, X. H., Feng, Z. Z., and Hao, G. Y.: Elevated ozone  
1167 concentration decreases whole-plant hydraulic conductance and disturbs water use  
1168 regulation in soybean plants, *Physiologia Plantarum*, 163, 183-195,  
1169 <https://doi.org/10.1111/ppl.12673>, 2018.

1170 Zheng, B., Tong, D., Li, M., Liu, F., Hong, C. P., Geng, G. N., Li, H. Y., Li, X., Peng, L. Q., Qi,  
1171 J., Yan, L., Zhang, Y. X., Zhao, H. Y., Zheng, Y. X., He, K. B., and Zhang, Q.: Trends in  
1172 China's anthropogenic emissions since 2010 as the consequence of clean air actions,  
1173 *Atmos. Chem. Phys.*, 18, 14095-14111, <https://doi.org/10.5194/acp-18-14095-2018>, 2018.

1174 Zhou, H., Yue, X., Lei, Y., Tian, C., Ma, Y., and Cao, Y.: Aerosol radiative and climatic effects  
1175 on ecosystem productivity and evapotranspiration, *Current Opinion in Environmental  
1176 Science & Health*, 19, <https://doi.org/10.1016/j.coesh.2020.10.006>, 2021.

1177 Zhou, H., Yue, X., Lei, Y., Tian, C., Zhu, J., Ma, Y., Cao, Y., Yin, X., and Zhang, Z.:  
1178 Distinguishing the impacts of natural and anthropogenic aerosols on global gross primary  
1179 productivity through diffuse fertilization effect, *Atmos. Chem. Phys.*, 22, 693-709,

1180 <https://doi.org/10.5194/acp-22-693-2022>, 2022.

1181 Zhou, H., Yue, X., Dai, H., Geng, G., Yuan, W., Chen, J., Shen, G., Zhang, T., Zhu, J., and Liao,  
1182 H.: Recovery of ecosystem productivity in China due to the Clean Air Action plan, *Nature*  
1183 *Geoscience*, 17, <https://doi.org/10.1038/s41561-024-01586-z>, 2024.

1184 Zhu, J. X., Jia, Y. L., Yu, G. R., Wang, Q. F., He, N. P., Chen, Z., He, H. L., Zhu, X. J., Li, P.,  
1185 Zhang, F. S., Liu, X. J., Goulding, K., Fowler, D., and Vitousek, P.: Changing patterns of  
1186 global nitrogen deposition driven by socio-economic development, *Nature*  
1187 *Communications*, 16, <https://doi.org/10.1038/s41467-024-55606-y>, 2025.

1188

1189